https://doi.org/10.5194/egusphere-2025-2665
Preprint. Discussion started: 10 July 2025

Evaluating the E3SMv2-MPAS Ocean-Sea Ice Coupled Unstructured Model in the Arctic: Atlantification Processes and Systematic Biases

Xinyuan Lv[1], Huizan Wang[1], Yu Cao[1], Kaijun Ren[1], Yangjun Wang[2] and Hao Ding[1]

[1]College of Meteorology and Oceanology, National University of Defense Technology, Changsha, 410073, China
[2]College of Advanced Interdisciplinary Studies, National University of Defense Technology, Nanjing, 211101, China

Correspondence to: Huizan Wang (wanghuizan@126.com) and Kaijun Ren (renkaijun@nudt.edu.cn)

Abstract. Advancing high-resolution Arctic ocean-sea ice modeling is critical for understanding polar amplification and improving climate projections but faces challenges from computational limits and cross-scale interactions. The simulation capabilities of the ocean-sea ice coupled model (E3SMv2-MPAS) from the Energy Exascale Earth System Model (E3SM) 2.1 for the Arctic sea ocean-sea ice system are systematically evaluated using multi-source observational data and model outputs. A latitudinally varying mesh (60 km in the Southern Hemisphere to 10 km in the Arctic) balances computational efficiency while integrating low-latitude oceanic influences. Unstructured meshes enhance geometric representation of Arctic straits, coupled with a suitable mesoscale eddy transport parameterization to establish a multi-scale simulation framework. Numerical results demonstrate E3SMv2-MPAS's superior Arctic simulation performance: (1) Accurate reproduction of spatial heterogeneity in sea ice concentration, thickness, and sea surface temperature, including their 1995–2020 trend patterns; (2) Successful reconstruction of three-dimensional thermohaline structures within the Atlantic Water layer, capturing Atlantic Water's decadal warming trends and accelerated Atlantification processes — specifically mid-layer shoaling, heat content amplification, and reduced heat transfer lag times in the Eurasian Basin. Persistent systematic biases are identified: 0.5–1 m sea ice thickness overestimation in the Canadian Basin compared to ICESat observations; Coordinated sea surface temperature/salinity underestimation and sea ice concentration overestimation in the Greenland and Barents Seas; Atlantic Water core temperature overestimation; Regional asymmetries in decadal thermohaline field evolution. These systematic biases may be attributed to three principal sources: inadequate representation of eddy dynamics, limitations in mixing parameterizations, and insufficient resolution of cross-scale interactions in key gateways (e.g., Fram Strait).

1 Introduction

The Arctic region has emerged as one of the most rapidly transforming components of the Earth system under contemporary climate change (Calvin et al., 2023). However, persistent gaps in oceanic observational networks, particularly the lack of systematic full-depth and pan-strait measurements across key Arctic gateways, have significantly constrained our

https://doi.org/10.5194/egusphere-2025-2665
Preprint. Discussion started: 10 July 2025

understanding of Arctic oceanic transport dynamics. To address these observational limitations, numerical modeling has become an indispensable tool (Wang et al., 2023). Of particular scientific significance is the thermohaline transport through Fram Strait – the principal conduit for Atlantic Water (AW) intrusion into the Arctic basins (Fu et al., 2023; Karami et al., 2021; Long et al., 2024). Recent studies highlight the necessity to quantify both the spatiotemporal evolution of AW-derived heat distribution across Arctic marginal seas and the relative contributions of different vertical heat flux mechanisms (Carmack et al., 2015b; Polyakov et al., 2020b). State-of-the-art global climate models (GCMs) provide critical insights into the evolving climate system under sustained global warming scenarios, enabling the investigation of multi-sphere interactions and their associated feedback mechanisms (Duarte et al., 2020; Hinrichs et al., 2021; Liang and Losch, 2018; Tian et al., 2022; Wassmann et al., 2015).

While climate models remain indispensable tools for deciphering Earth system dynamics (Landrum and Holland, 2020), their representation of Arctic processes exhibits persistent uncertainties that challenge predictive capabilities (Pan et al., 2023). Systematic biases plague the simulation of critical Arctic phenomena, including amplified warming rates, sea ice retreat patterns, and AW layer evolution (Heuzé et al., 2023; Khosravi et al., 2022; Muilwijk et al., 2023; Shu et al., 2019). These limitations persist across successive model generations, as evidenced by Coupled Model Intercomparison Project Phase 5 (CMIP5) and Phase 6 (CMIP6) revealing substantial errors in Arctic three-dimensional thermohaline structure reproduction (Khosravi et al., 2022; Shu et al., 2019). There are mainly four common biases of contemporary models in the Arctic include: (1) Overestimated AW layer thickness and depth. This systematic vertical structure misrepresentation persists across model generations, from early Arctic Ocean Model Intercomparison Project (AOMIP) simulations (Holloway et al., 2007) through the Coordinated Ocean-ice Reference Experiments, phase II (CORE-II; Ilıcak et al., 2016), and the most widely used CMIP5/CMIP6 ensembles (Heuzé et al., 2023; Khosravi et al., 2022; Shu et al., 2019). Among 41 CMIP5 models evaluated by Shu et al., (2019), 22% failed basic AW identification criteria, while the remaining 32-model mean overestimated AW layer vertical extent compared to observational benchmarks. CMIP6 shows limited improvement, with multi-model mean AW upper boundaries erroneously positioned at ~400 m depth in the Nansen Basin – deeper than observed values – and excessive thickness extending to seafloor regions in some regions (Khosravi et al., 2022). (2) Cold bias in AW core temperatures. The Alfred Wegener Institute coupled climate model (AWI-CM1) exhibits thermal underestimation at 200–600m depths in Eurasian Basin simulations (Hinrichs et al., 2021), consistent with CMIP6's 0.4°C cold bias relative to hydrographic climatologies (Heuzé et al., 2023). (3) Failure to capture AW warming trends. CMIP5 models collectively underestimate observed decadal temperature variability, with no model replicating post-2000 acceleration in AW warming (Shu et al., 2019). (4) Underestimated "Atlantification" (referring to the Arctic Ocean water properties becoming increasingly akin to the warmer and saltier Atlantic water). While models project gradual boreal water encroachment in the Barents Sea by 2100 (Wassmann et al., 2015), observational analyzes suggest this regime shifts is likely to occur at a faster pace (Lind et al., 2018). Discrepancies extend to sea ice thermodynamics, where Seasonal Forecast System 5 (SEAS5) simulations yield only 10–20 cm winter ice production decline (Polyakov et al., 2022), versus 78–93 cm observed losses (Polyakov et al., 2020b).

https://doi.org/10.5194/egusphere-2025-2665
Preprint. Discussion started: 10 July 2025

There are numerous and complex reasons that lead to the common deviations in models when simulating the AW. These challenges can be categorized into four primary domains: (1) Insufficient horizontal resolution (>50 km in most CMIP6 models) fails to resolve critical boundary currents and mesoscale eddies (Hinrichs et al., 2021); (2) Unrealistic Atlantic-Arctic exchange through Fram Strait (Hinrichs et al., 2021); (3) Parameterization deficiencies, including the incorrect representation of horizontal advection and vertical mixing (Lind et al., 2018); (4) Imperfect knowledge of ocean-sea ice-atmosphere triadic feedbacks, especially during winter convection events, hampers accurate simulation of AW ventilation processes (Heuzé et al., 2023). To advance model fidelity and reduce uncertainty sources, comprehensive investigations into systematic model biases are imperative (Hinrichs et al., 2021; Pan et al., 2023).

Current numerical simulations for polar regions are primarily based on structured grid models. However, the inherent limitations of structured grids, particularly the singularity at the North Pole and meridional convergence artifacts, fundamentally constrain their capacity to represent Arctic-specific physical processes (Liu et al., 2016). These geometric constraints not only distort parameterization schemes but also introduce systematic biases in both regional and decadal-scale simulations. While global high-resolution configurations could theoretically mitigate such issues, their prohibitive computational costs render them impractical for climate-scale applications (Golaz et al., 2019). This technological impasse has driven the development of two complementary approaches: (1) Nested grid systems: Though offering advantages in temporal discretization flexibility and geometric simplification, their implementation introduces nontrivial challenges in mass conservation, interface coupling fidelity, and numerical noise suppression (Hoch et al., 2020). (2) Unstructured mesh: By enabling localized resolution enhancement in dynamically critical zones while maintaining coarse resolutions elsewhere, these meshes eliminate the need for explicit nesting procedures (Scholz et al., 2019). Their continuous spatial adaptability allows direct resolution of sub-mesoscale processes without compromising computational efficiency (Wang et al., 2018).

The application of variable-resolution models with a global unstructured meshes offers distinct advantages for Arctic Ocean studies. By employing high-resolution meshes over the Arctic region, these configurations enable accurate simulation of energy exchange processes across narrow critical channels (e.g., Fram Strait, Bering Strait, Barents Sea Opening and Davis Strait). Coarser resolutions in other domains maintain computational efficiency while preserving connectivity between the Arctic and extratropical regions (Wang et al., 2018). Among global implementations, two widely adopted models are the Finite-Volume Coastal Ocean Model (FVCOM; Chen et al., 2016) and the Finite-Element Sea ice-Ocean circulation Model (FESOM; Danilov et al., 2017). In Arctic studies, FVCOM predominantly operates as a regional model, as evidenced by its frequent implementation in localized domains (e.g., Zhang et al., 2016). This regional focus aligns with FVCOM's original design paradigm prioritizing coastal and shelf-sea dynamics through its finite-volume discretization scheme. In contrast, FESOM has been predominantly implemented as a global model in Arctic studies, where its implementation has demonstrated unprecedented skill in simulating Arctic intermediate water dynamics (Danilov et al., 2017; Wang et al., 2018; Wekerle et al., 2013). Notably, Wang et al., (2018) established that FESOM's (a relatively low resolution, ~24 km in the Arctic) outperforms a set of the then state-of-the-art structured-grid models evaluated by Ilıcak et al., (2016), particularly in correcting systematic AW core biases.

https://doi.org/10.5194/egusphere-2025-2665
Preprint. Discussion started: 10 July 2025

As a more recent modeling framework relative to FESOM and FVCOM, the Model for Prediction Across Scales (MPAS) remains in the nascent phase of Arctic performance evaluation (Ringler et al., 2013), particularly regarding its capacity to simulate intermediate water masses and Atlantification processes. The Energy Exascale Earth System Model (E3SM), evolved from the Community Earth System Model (CESM), incorporates MPAS-Ocean and MPAS-Seaice as its ocean and sea ice components. Initial assessments using E3SMv1's ocean-sea ice coupled configuration (60to10 km variable resolution) demonstrate promising skill in reproducing pan-Arctic freshwater budgets, gateway current exchanges, and vertical hydrographic profiles (Veneziani et al., 2022). Persistent errors in sea ice thickness (SIT) distribution and upper 100 m stratification emerge across resolutions, suggesting common structural models deficiencies rather than discretization artifacts. However, their diagnostic lack the rigorous validation metrics employed by Wang et al., (2018) for FESOM's AW representation. Existing assessments predominantly rely on pan-Arctic-basin-averaged diagnostics, obscuring critical vertical and regional heterogeneities in intermediate AW layer dynamics (Veneziani et al., 2022).

This study presents a tripartite evaluation framework for the coupled system of MPAS-Ocean and MPAS-Seaice in E3SM version 2 (E3SMv2-MPAS), which compares it with the observational datasets and high-resolution model outputs from CMIP6 and the Ocean Model Intercomparison Project Phase 2 (OMIP2) to systematically assess MPAS's capacity to address persistent Arctic AW biases. In addition, we conduct a comprehensive assessment of Arctic sea ice dynamics, surface layer hydrographic properties and three-dimensional thermohaline profile evolution, with particular emphasis on their respective strengths, limitations, and potential sources of uncertainty. Innovatively, this work implements a multi-layer connectivity analysis examining cross-layer interactions between surface (10 m) and intermediate (400 m) depths.

The subsequent sections are structured as follows: Section 2 provides comprehensive documentation of the E3SMv2-MPAS configuration and validation datasets. Section 3 and Section 4 conduct rigorous multi-faceted analyzes of Arctic-specific simulations, employing both domain-wide diagnostics and sub-regional decomposition approaches. These sections also discuss remaining challenges in polar ocean-sea ice modeling, and proposes targeted development pathways for next-generation Earth system models. The concluding Section 5 synthesizes key findings.

2 Model Configurations and Data

2.1 Model Configuration

Veneziani et al., (2022) demonstrated that refining mesh resolution from 10 km to 6 km triples computational costs without yielding significant improvements in simulation fidelity. Their findings suggest that resolving the local Rossby radius of deformation across most Arctic regions necessitates resolutions ≤3 km — a requirement currently constrained by prohibitive computational demands. The model configuration in this paper is described as follows. To address the trade-off between high-resolution requirements and computational constraints, our study employs a variable-resolution unstructured mesh featuring a meridional transition from 60 km resolution in the Southern Hemisphere to 10 km in the Arctic domain (hereafter 60to10 km; Fig. 1a). This adaptive meshing approach optimizes computational efficiency while resolving critical processes:

https://doi.org/10.5194/egusphere-2025-2665
Preprint. Discussion started: 10 July 2025

Antarctic coastal regions (80°S–90°S) maintain 25 km resolution to capture fine-scale dynamics; The North Atlantic sector demonstrates strategically prioritized mesh refinement, transitioning from 20 km to 10 km resolution earlier than its Pacific counterpart to guarantee at least 15 km resolution in the Gulf Stream extension region (~40°N; Veneziani et al., 2022); The North Pacific configuration maintains computational efficiency while achieving approximately 10 km resolution in the subpolar North Atlantic sector adjacent to the Arctic Ocean (north of 50°N).

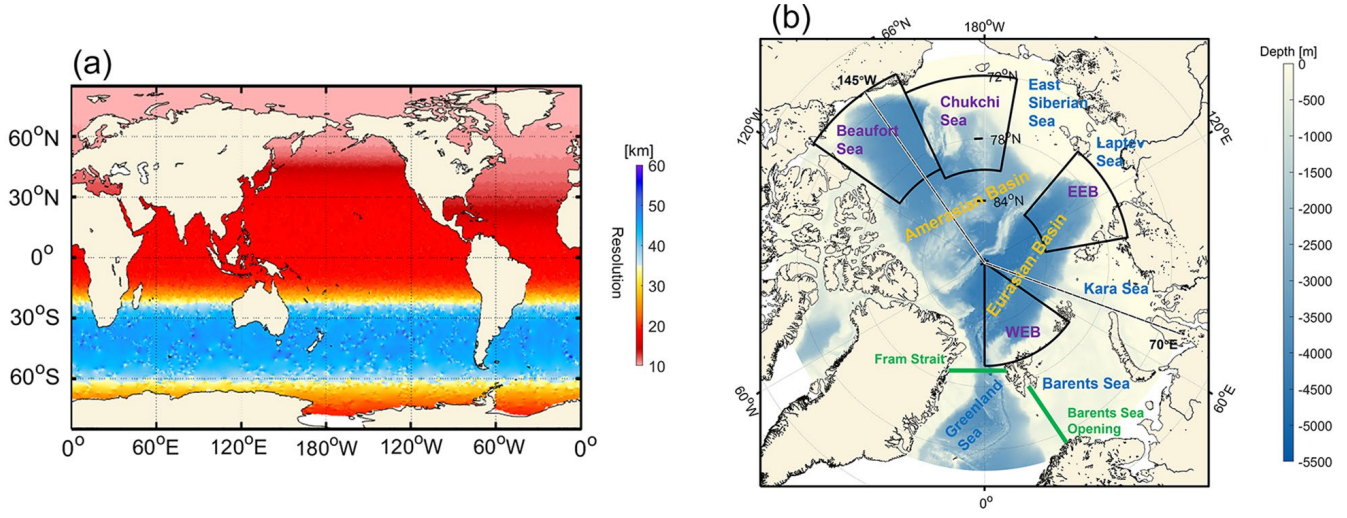

Figure 1. (a) Geographical distribution of grid cell size (km) of the E3SMv2-MPAS framework. (b) Bathymetry from the ETOPO 2022 and key basins/straits north of 60°N. EEB and WEB refer to the eastern and the western Eurasian Basin respectively. The black dashed transect along 70°E and 145°W (crossing the North Pole) denotes the location of the transect shown in Fig. 14.

Numerical stability is achieved through a 5-minute baroclinic time step for ocean dynamics and a 2:1 ratio of sea ice thermodynamic to dynamic time-stepping. Vertical mixing processes are parameterized using the K-profile scheme (KPP; Large et al., 1994). For mesoscale eddy representation, we implement a spatially varying Gent-McWilliams (GM) parameterization, incorporating both bolus advection and Redi isopycnal diffusion components (Gent and Mcwilliams, 1990). The eddy diffusivity coefficient (κ) exhibits latitudinal dependence: 300 $m^2\ s^{-1}$ in high-resolution Arctic regions (<20 km grid spacing) to maintain moderate mixing intensity, transitioning linearly to 1800 $m^2\ s^{-1}$ in low-resolution zones (>30 km grid spacing) to compensate for unresolved eddy fluxes. The specific configurations of MPAS-Ocean and MPAS-Seaice within the E3SMv2, including their coupling mechanisms, have been comprehensively documented in Turner et al., (2022) and Golaz et al., (2022).

In addition to the ocean and sea ice components, the atmospheric and river modules in E3SMv2-MPAS are forced by the JRA55-do (v1.5; Tsujino et al., 2018) from the Japan Meteorological Agency (JMA). This dataset has high spatiotemporal resolution (3-hourly temporal and 0.5625° spatial resolution) and spans the period from 1958 to 2020. Sea surface salinity (SSS) is relaxed toward Polar science center Hydrographic Climatology (PHC) 3.0 climatology (Steele et al., 2001) with an annual restoring timescale. The initial conditions for the MPAS-Ocean and MPAS-Seaice components (including salinity, temperature, sea surface height gradients, and surface velocities) were sourced from the E3SMv2 predefined benchmark case

https://doi.org/10.5194/egusphere-2025-2665
Preprint. Discussion started: 10 July 2025

files (specifically ocean.ARRM60to10.180715.nc). These fields were generated through a prior forward simulation of the MPAS-Ocean model. This initial state is intrinsically consistent with E3SM's dynamical core, having undergone a spin-up process within the MPAS-Ocean framework prior to being archived as a standard case. Following the configuration of forcing and initial conditions (see Fig. 2 for parameter details), E3SMv2-MPAS achieves rapid surface state alignment with observational benchmarks during initial integration (surface temperature anomalies <5% within the first month). The simulation periods explicitly configured in this study are 1960–1980 and 1995–2020. The exclusion of intermediate years (1981–1994) preserves computational resources while maintaining climatological fidelity, as verified through overlapping-period consistency checks (1995–2020).

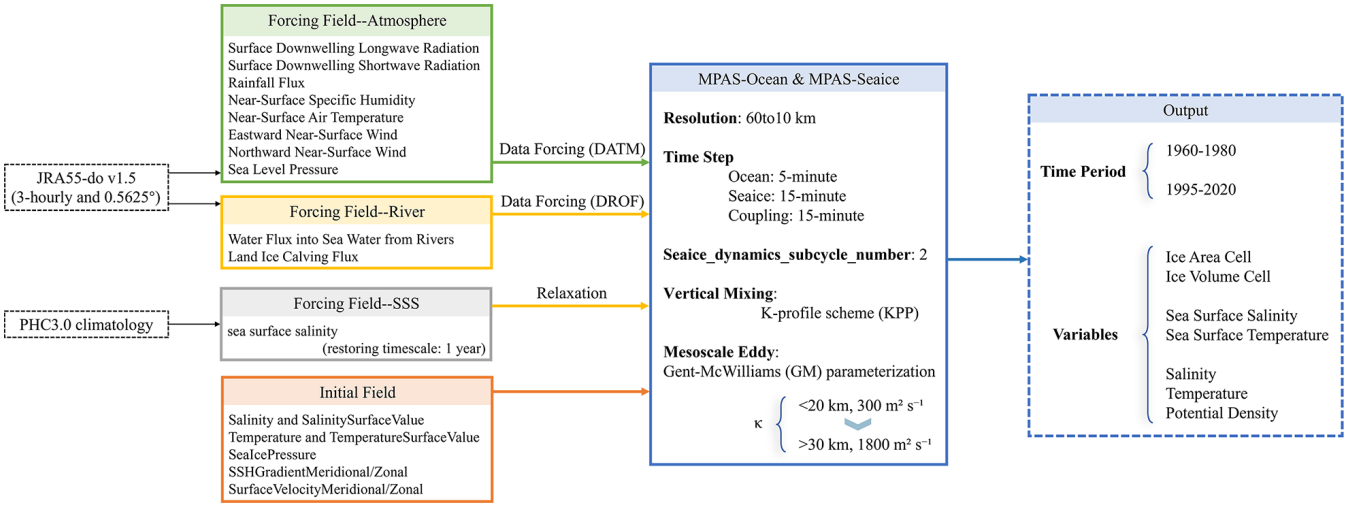

Figure 2. Configuration details for E3SMv2-MPAS: forcing/initial conditions, runtime settings, and output fields.

2.2 Evaluation Datasets

2.2.1 Sea Ice Concentration and Thickness

To comprehensively evaluate sea ice concentration (SIC) performance, both the observations and reanalysis data were adopted for validation. SIC datasets used here include: (1) Passive microwave remote sensing data: Sourced from the National Oceanic and Atmospheric Administration (NOAA) / National Snow and Ice Data Center (NSIDC) Climate Data Record (Version 4; Meier et al., 2021) with a spatial resolution of 25 km × 25 km; (2) HadISST1 data: Provided by the UK Met Office Hadley Centre (Rayner et al., 2003) at 1° × 1° resolution; (3) ERA5 reanalysis: Generated by the European Centre for Medium-Range Weather Forecasts (ECMWF; Hersbach et al., 2020) at 0.25° × 0.25° resolution.

For sea ice thickness (SIT) validation, we utilize four key datasets: (1) Pan-Arctic Ice-Ocean Modeling and Assimilation System (PIOMAS; Zhang and Rothrock, 2003): This reanalysis product, extensively validated against satellite and in situ observations, provides reliable Arctic SIT spatial distributions and long-term trends (Laxon et al., 2013; Schweiger et al., 2011; Stroeve et al., 2014). (2) PIOMAS-20C reanalysis (Schweiger et al., 2019): Driven by ECMWF's atmospheric reanalysis of the 20th century (ERA-20C) and calibrated with historical in situ/aircraft measurements, this dataset enables

https://doi.org/10.5194/egusphere-2025-2665
Preprint. Discussion started: 10 July 2025

analysis of pre-satellite-era SIT variability (1960–1980). (3) Ice, Cloud, and Land Elevation Satellite-1 (ICESat-1; 2003–2008): Equipped with the Geoscience Laser Altimeter System (GLAS; Zwally et al., 2002), enabling pioneering lidar-based SIT retrievals. (4) ICESat-2 (2018–2020): Employing the Advanced Topographic Laser Altimeter System (ATLAS; Petty et al., 2020) to acquire high-resolution three-dimensional SIT measurements, significantly enhancing small-scale ice monitoring capabilities.

2.2.2 Sea Surface Temperature and Salinity

Sea surface temperature (SST) validation dataset is NOAA's 1/4° Daily Optimum Interpolation Sea Surface Temperature (OISST; Huang et al., 2021) dataest, represents a long-term climate data record integrating multi-platform observations from satellites, ships, buoys, and Array for real-time geostrophic oceanography (Argo) floats. Spatially continuous global SST fields are reconstructed using optimal interpolation to fill data gaps.

For sea surface salinity (SSS), the National Aeronautics and Space Administration (NASA) sponsored Optimum Interpolation Sea Surface Salinity (OISSS; Melnichenko et al., 2016) dataest was applied. The product integrates multi-satellite observations from Aquarius, Soil Moisture Active Passive (SMAP), and Soil Moisture and Ocean Salinity (SMOS) through optimal interpolation. Continuous 2011-present data are generated through cross-satellite bias correction and spatial filtering, with SMOS data filling SMAP gaps.

2.2.3 Three-Dimensional Thermohaline

The World Ocean Atlas 2023 (WOA23; Locarnini et al., 2024; Reagan et al., 2024) served as the primary validation dataset for three-dimensional thermohaline properties. WOA23 produces high-resolution global climatological temperature and salinity fields via interpolation of historical observations (Argo floats, ship-based measurements, satellite data), covering three periods in this study: 1991–2020, 1995–2004, and 2005–2014.

To assess long-term thermohaline evolution (1960–1980 vs. 2000–2020), the UK Met Office's EN.4.2.2 dataest (Good et al., 2013) was combined. EN.4.2.2 assimilates multi-source in situ data (ship observations, Argo floats, Conductivity-Temperature-Depth (CTD) profilers, moored buoys), applies rigorous quality control, and reconstructs 1° × 1° gridded temperature/salinity fields spanning 0–5500 m depth from 1900 onward.

Furthermore, annual mean temperature and salinity profiles (1970–2017) over the East Eurasian Basin, the West Eurasian Basin, the Chukchi Sea, and the Beaufort Gyre from Muilwijk et al., (2023) were included. These data derive from Russian, American, Canadian, and European expeditions, including ship/aircraft surveys, manned drifting stations, autonomous buoys, and submarine measurements.

To evaluate E3SMv2-MPAS performance among models, comparisons were made against CMIP6's 13 high-resolution models (Muilwijk et al., 2023) and five high-low resolution model pairs from OMIP2 (Wang et al., 2024), covering 1995–2014 and 1958–2018, respectively (see Table 1 and references for details).

https://doi.org/10.5194/egusphere-2025-2665
Preprint. Discussion started: 10 July 2025

Table 1. Numerical implementations of E3SMv2-MPAS, E3SM-Arctic-OSI (Veneziani et al., 2022), 13 CMIP6 models (Muilwijk et al., 2023), and 5 OMIP2 model pairs (Wang et al., 2024), detailing grid type, horizontal resolution in Arctic, and vertical grid.

	Model	Grid type	Horizontal resolution in Arctic (km)	Vertical grid (No. of levels)
E3SMv2	E3SMv2-MPAS	Unstructured	10	z (80)
E3SMv1	E3SM-Arctic-OSI	Unstructured	10	z (80)
CMIP6	BCC-CSM2-MR	Tripolar	54	z (40)
	CAMS-CSM1-0	Tripolar	54	z (50)
	CESM2	Rotated	41	z (60)
	CanESM5	Tripolar	50	z (45)
	GFDL-CM4	Tripolar	9	ρ-z* (75)
	GFDL-ESM4	Tripolar	18	ρ-z* (75)
	IPSL-CM6A-LR	Tripolar	49	z* (75)
	GISS-E2-1-H	Regular	46	ρ-z-σ (32)
	MIROC6	Tripolar	39	z-σ (62)
	MPI-ESM1-2-HR	Tripolar	36	z (40)
	MRI-ESM2-0	Tripolar	39	z* (60)
	NorESM2-LM	Tripolar	38	ρ-z (53)
	UKESM1-0-LL	Tripolar	50	z* (75)
OMIP2	ACCESS-MOM_3.6km	Tripolar	3.6	z* (70)
	ACCESS-MOM_9km	Tripolar	9	z* (50)
	AWI-FESOM_4.5km	Unstructured	4.5	z (47)
	AWI-FESOM_24km	Unstructured	24	z (47)
	CMCC-NEMO_3.2km	Tripolar	3.2	z (98)
	CMCC-NEMO_51km	Tripolar	51	z (50)
	FSU-HYCOM_3.6km	Tripolar	3.6	ρ-z-σ (36)
	FSU-HYCOM_32km	Tripolar	32	ρ-z-σ (41)
	IAP-LICOM_6.8km	Tripolar	6.8	η (55)
	IAP-LICOM_72km	Tripolar	72	η (30)

https://doi.org/10.5194/egusphere-2025-2665
Preprint. Discussion started: 10 July 2025

Additionally, three-dimensional thermohaline outputs from E3SMv1 (60to10 km resolution; 2005–2016 climatology; Veneziani et al., 2022) were analyzed. Golaz et al., (2022) explicitly confirm that the oceanic component MPAS-Ocean in E3SMv2 contains no substantial improvements over its E3SMv1 predecessor. Key differences between E3SM-Arctic-OSI (Veneziani et al., 2022) and E3SMv2-MPAS involve GM eddy diffusivity coefficient (κ) settings. E3SM-Arctic-OSI disables GM parameterization (κ=0) in Arctic regions, while E3SMv2-MPAS maintains moderate mesoscale diffusion. Though GM deactivation enhances frontal sharpness (e.g., ice-edge zones and thermal gradients), most Arctic regions feature first baroclinic Rossby radii <10 km (Nurser and Bacon, 2014). At 10 km resolution, unresolved mesoscale eddies may cause transport deficiencies, non-physical gradients, and circulation distortions (e.g. anomalous sea ice distributions and systematic thermohaline circulation biases).

2.2.4 Atlantic Water Core

Observed Atlantic Water (AW) core temperature and depth data were sourced from Richards et al., (2022), comprising 55,841 profiles (1977–2018). AW core was defined as the warmest layer within salinity >34.7 PSU profiles. To ensure accuracy, only profiles exceeding 500 m depth with sampling starting above 100 m were retained. Raw profiles were smoothed using an 80 m vertical moving average (40 m window) to remove spikes caused by thermohaline intrusions and eddies while preserving overall thermal structure.

Wang et al., (2024)'s OMIP2 dataset includes AW core temperature (defined as maximum temperature in water columns over seafloor depths >150 m; 2006–2017) from five high-low resolution model pairs. This dataset is employed to benchmark E3SMv2-MPAS's AW core temperature simulations against multi-model ensembles.

3 Arctic Physical System States

3.1 Sea Ice Characterization

This study focuses on the Arctic region, systematically evaluating the simulation performance of the E3SMv2-MPAS coupled model for sea ice concentration (SIC), sea ice thickness (SIT), sea surface temperature (SST), and sea surface salinity (SSS) at first. Through comparisons with multi-source observational datasets and reanalysis products, combined with climate-state analysis (1995–2020) and trend diagnostics across two periods (1960–1980 and 1995–2020), model strengths and limitations in polar environmental simulations are identified.

Multi-dataset validation using NSIDC satellite remote sensing (Meier et al., 2021), Hadley in situ assimilation (Rayner et al., 2003), and ERA5 reanalysis (Hersbach et al., 2020) demonstrates that E3SMv2-MPAS effectively captures spatial heterogeneity in Arctic SIC climatology (Fig. 3a–g). Consistent spatial bias patterns are observed across datasets, with persistent positive bias centers (ΔSIC>0.3) identified along the southwestern Greenland Sea shelf margin and the northern Barents Sea slope. Notably, E3SMv2-MPAS exhibits superior performance relative to CMIP6 ensemble members, demonstrating smaller spatial bias magnitudes than most models (Long et al., 2021). E3SMv2-MPAS successfully

https://doi.org/10.5194/egusphere-2025-2665
Preprint. Discussion started: 10 July 2025

reproduces SIC seasonal cycles and interannual variability, maintaining root mean square errors (RMSE) values of 0.040, 0.052, and 0.051 against NSIDC, Hadley, and ERA5 datasets respectively (Fig. 3h). This validates the dynamic framework's effectiveness in capturing sea ice-atmosphere coupling mechanisms. However, the asymmetric seasonal biases in E3SMv2-MPAS are identified, which shows: systematic winter overestimation contrast with moderate summer underestimation (primarily compared with NSIDC), suggesting potential improvements needed in simulating ice-albedo feedback and melt pond dynamics. Trend analysis confirms the model's climate response capability. During the rapid decline period (1995–2020), E3SMv2-MPAS accurately captures accelerated SIC reduction trends, showing better agreement with NSIDC observations than Hadley and ERA5 products. For the weak-trend period (1960–1980), the model reproduces quasi-stable sea ice coverage characteristics while maintaining overestimated seasonal variability amplitudes. The accelerated SIC decline in the recent period compared to historical decades highlights the model's ability to replicate trend amplification under intensified forcing, thereby bolstering confidence in its scenario-dependent projections.

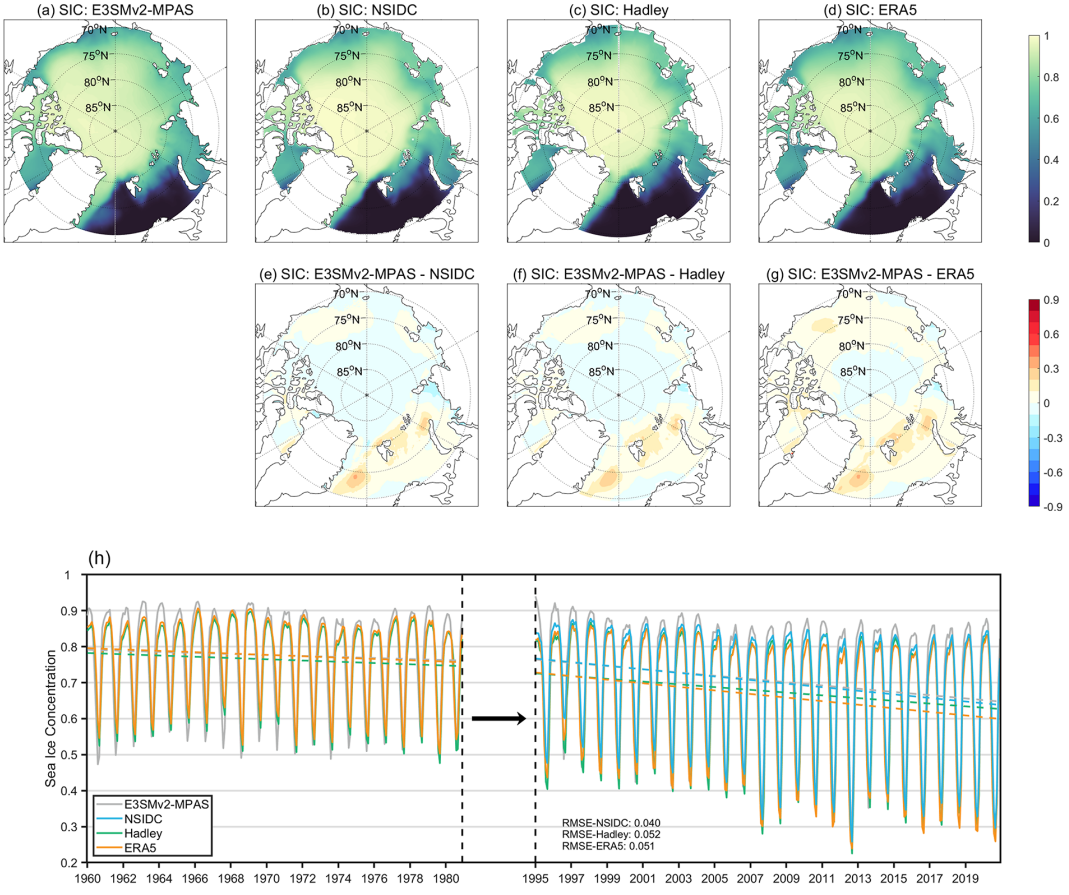

Figure 3. (a–d) 1995–2020 climatological mean sea ice concentration (SIC) spatial distributions: (a) E3SMv2-MPAS simulations, (b) NSIDC observational product, (c) Hadley Centre HadISST data, (d) ERA5 reanalysis. (e–g) SIC bias fields: (e) E3SMv2-MPAS vs. NSIDC, (f) E3SMv2-MPAS vs. Hadley, (g) E3SMv2-MPAS vs. ERA5. (h) Pan-Arctic (70°N–90°N) mean SIC time series for 1960–1980 and 1995–2020, with dashed lines indicating linear trends (E3SMv2-MPAS: gray; NSIDC: blue; Hadley: green; ERA5: orange) derived from least-squares regression.

https://doi.org/10.5194/egusphere-2025-2665
Preprint. Discussion started: 10 July 2025

Beyond SIC, SIT serves as a critical parameter governing sea ice dynamics, with its simulation accuracy directly modulating the spatiotemporal heterogeneity of ice volume. We systematically quantify E3SMv2-MPAS's capability in reproducing SIT spatiotemporal evolution (Fig. 4). Comparative analysis demonstrates the model effectively captures Arctic SIT spatial gradients (Fig. 4a–c). Although the model generally overestimates SIT, the time series analysis successfully simulates continuous thinning from ~1.8 m to ~1.3 m during 1995–2020 (Fig. 4d). Notably, however, the simulated thinning rates remain slightly lower than PIOMAS results. Stable RMSE values (~0.37) throughout this period confirm robust simulation of long-term SIT evolution. For the pre-satellite era (1960–1980), evaluation using PIOMAS-20C shows E3SMv2-MPAS reproduces the 6-year cyclic "increase-decrease-increase" SIT fluctuations during 1960–1978 (Fig. 4d). While PIOMAS-20C shows no statistically significant SIT trend during 1960–1980, E3SMv2-MPAS simulates a pronounced thickening trend in this period, potentially linked to its systematic overestimation of regional ice thickness in areas like the Beaufort Sea (Fig. 4c). Nevertheless, across the multi-decadal scale (1960–2020), this coupled system demonstrates a reasonable representation of Arctic sea ice responses to climate forcing.

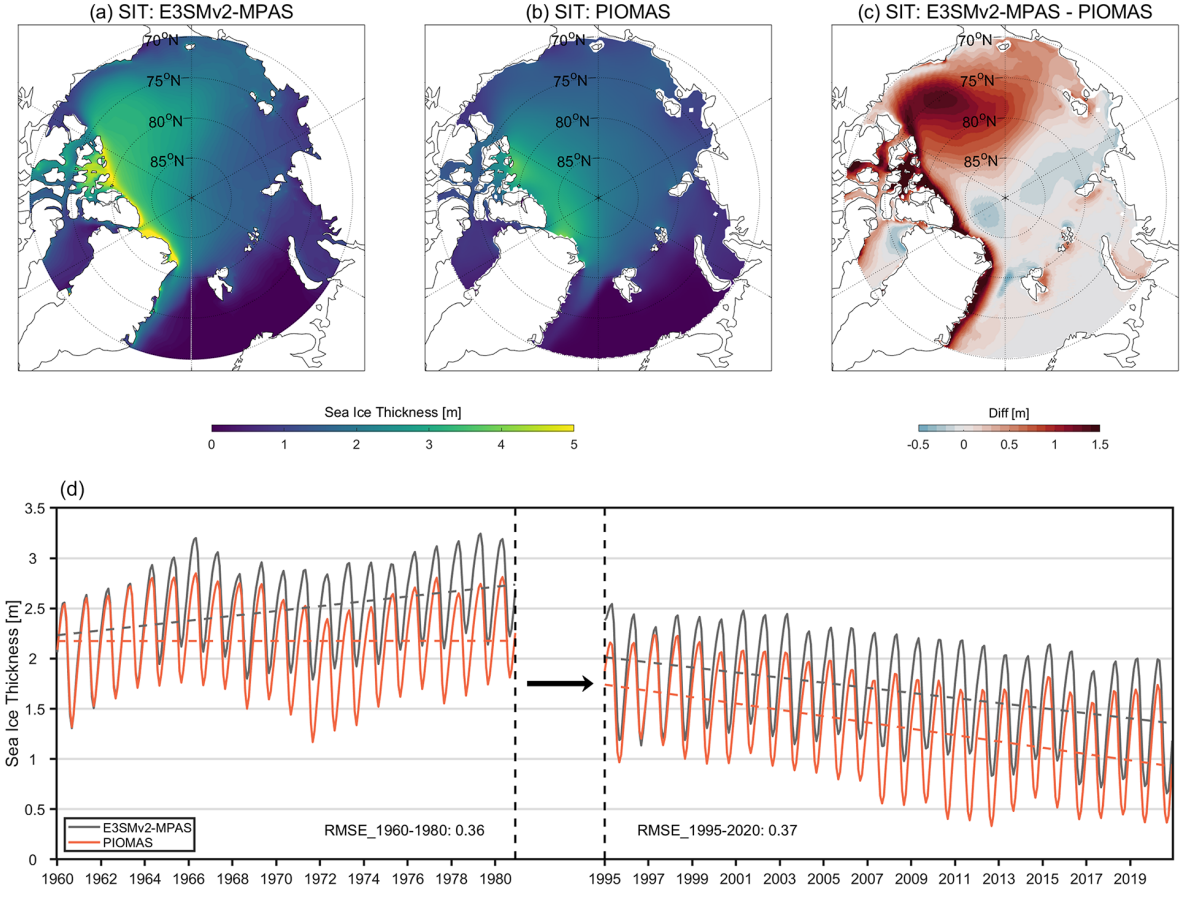

Figure 4. (a–b) 1995–2020 climatological mean sea ice thickness (SIT) spatial distributions: (a) E3SMv2-MPAS, (b) PIOMAS. (c) SIT bias field: E3SMv2-MPAS vs. PIOMAS. (d) Pan-Arctic (70°N–90°N) mean SIT time series for 1960–1980 and 1995–2020, with dashed lines indicating linear trends (E3SMv2-MPAS: black; PIOMAS: red) derived from least-squares regression.

https://doi.org/10.5194/egusphere-2025-2665
Preprint. Discussion started: 10 July 2025

Spatial analysis identifies significant zonal positive biases (ΔSIT>1.5 m) along the eastern and northern Greenland Sea shelf and the Canadian Archipelago (Fig. 4c). Considering PIOMAS's known limitations in overestimating thin ice while underestimating thick ice (Laxon et al., 2013; Schweiger et al., 2011), additional validation using ICESat altimetry data (Petty et al., 2023) is conducted (Fig. 5). Case studies of specific months (February 2005, October 2005, October 2006, March 2007, March 2019, October 2019) show improved agreement with ICESat observations in the Canadian Archipelago and Greenland coastal regions compared to PIOMAS. Persistent 0.5–1 m positive biases in the Canadian Basin interior are hypothesized to originate from an overestimated intensity of the Beaufort Gyre in E3SMv2-MPAS, potentially enhancing sea ice convergence processes.

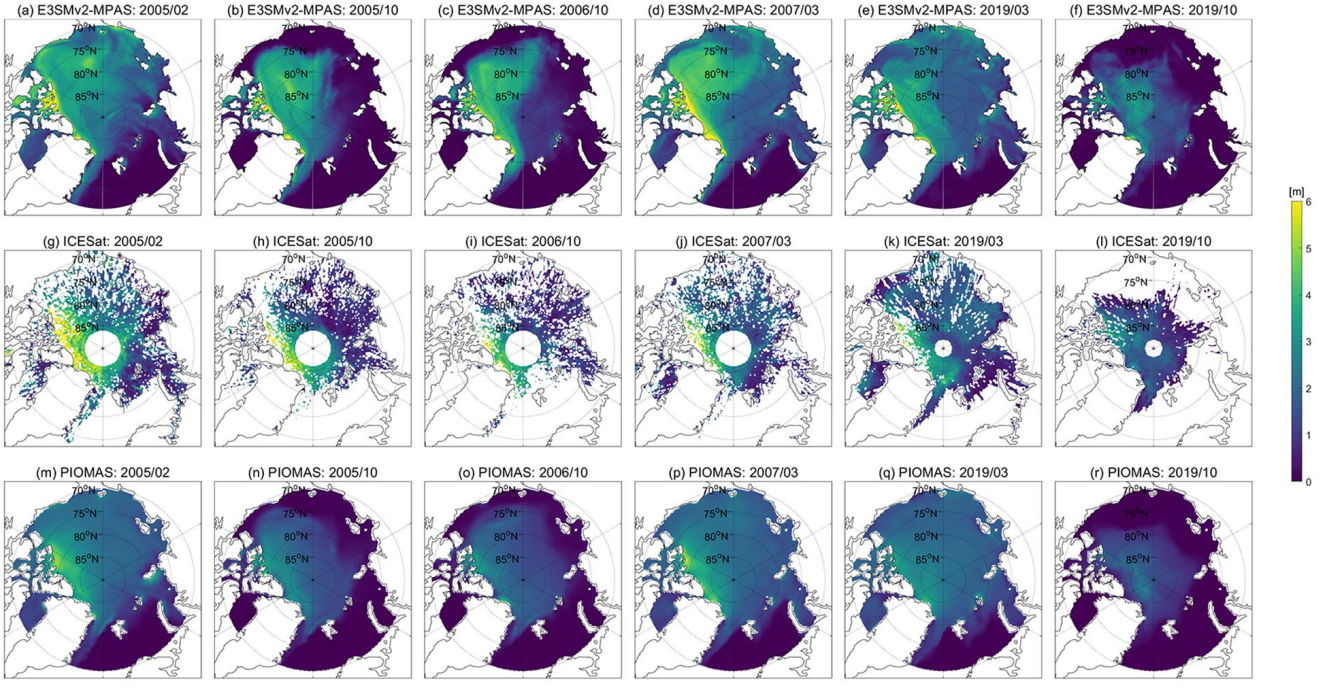

Figure 5. Seasonal sea ice thickness spatial distributions. Rows: (1) E3SMv2-MPAS, (2) ICESat, (3) PIOMAS. Columns: (1) February 2005, (2) October 2005, (3) October 2006, (4) March 2007, (5) March 2019, (6) October 2019.

3.2 Surface Thermohaline Signatures

SST and SSS engage in complex bidirectional coupling with the atmosphere-ice system through ice/atmosphere-ocean interfacial energy-mass exchange processes. This section evaluates the spatiotemporal co-variability of SST/SSS to elucidate E3SMv2-MPAS's representation of ocean-sea ice-atmosphere interaction mechanisms.

OISST-based validation demonstrates E3SMv2-MPAS accurately reproduces key Arctic SST spatial patterns: (1) temperature gradients decreasing from shelves to central basins, and (2) warm-core features in southern Barents Sea open waters (Fig. 6a–c). Systematic regional biases are identified: the cold biases in the Greenland Sea (ΔSST≈-2–0°C) spatially correlate with an overestimation of SIC in the same region, while positive deviations (ΔSST≈0–2°C) occur near Svalbard's

https://doi.org/10.5194/egusphere-2025-2665
Preprint. Discussion started: 10 July 2025

western coast and the Eurasian continental margins. Notably, continental coastal biases are spatially decoupled from Atlantic inflow pathways, with formation mechanisms likely associated with inaccurate vertical mixing processes stemming from stratification stability biases in shelf regions. E3SMv2-MPAS successfully captures Arctic SST warming trends during the 1995–2020 period, showing high consistency with OISST in accelerated trend characteristics (Fig. 6d). Seasonal cycle and interannual variability simulations remain within acceptable error ranges (RMSE=0.24), confirming appropriate responses to surface thermal forcing. Furthermore, the model accurately captures both the pronounced SST increase and accelerated decadal warming trend during 1995–2020 relative to the 1960–1980 baseline period. These simulated changes show a strong coupling with the accelerated decline in SIC and SIT concurrently (Figs. 3h, 4d).

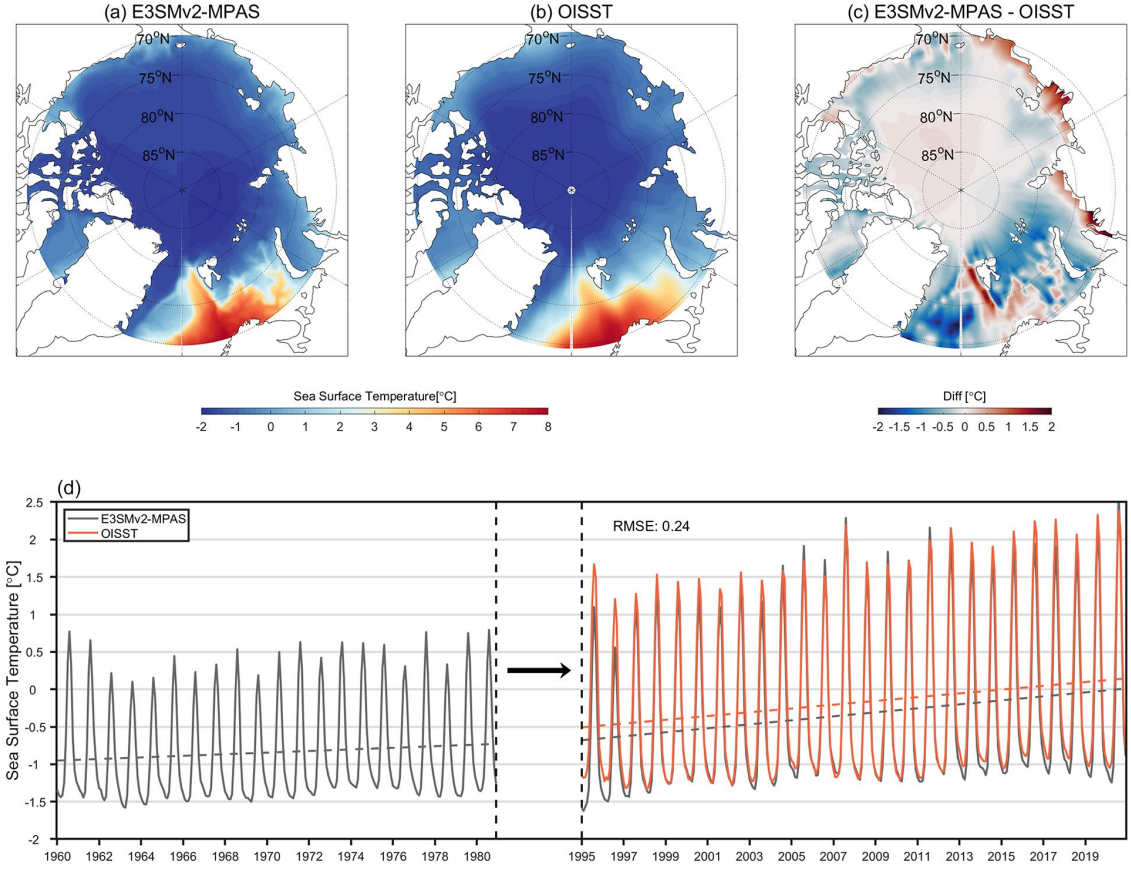

Figure 6. (a–b) 1995–2020 climatological mean sea surface temperature (SST) spatial distributions: (a) E3SMv2-MPAS, (b) OISST. (c) SST bias field: E3SMv2-MPAS vs. OISST. (d) Pan-Arctic (70°N–90°N) mean SST time series for 1960–1980 and 1995–2020, with dashed lines indicating linear trends (E3SMv2-MPAS: black; OISST: red) derived from least-squares regression.

E3SMv2-MPAS demonstrates comparatively weaker performance in SSS simulation versus sea ice and SST variables. Spatially heterogeneous biases are observed: negative deviations (ΔSSS=-0–1 PSU) in the Barents and Greenland Seas contrast with pronounced positive biases (ΔSSS=2–5 PSU) in the Beaufort Sea and the Kara-Beaufort shelf regions (Fig. 7a–c). The 3 PSU overestimation in the Beaufort Sea aligns with advanced assimilation model (such as HYCOM and

https://doi.org/10.5194/egusphere-2025-2665
Preprint. Discussion started: 10 July 2025

GLORYS12) biases reported by Hall et al., 2021, suggesting common limitations in Arctic shelf freshwater transport representation. Specifically, inadequate parameterization of surface freshwater budgets and associated processes (e.g., precipitation-evaporation fluxes, river discharge, and ice-ocean interactions) may constrain freshwater cycle simulations (Wang et al., 2024). The Beaufort Sea SIT overestimation identified previously (Fig. 4a–c) potentially exacerbates salinity biases through reduced freshwater release (Kelly et al., 2019). If the intensity of the Beaufort Gyre is overestimated (as discussed in Section 3.1), enhanced freshwater retention could impede westward shelf transport to the Kara Sea, potentially driving salinity overestimation in the Kara-Beaufort shelf. Despite spatial biases, E3SMv2-MPAS demonstrates credible simulation of seasonal cycle phasing and amplitude in the Barents Sea SSS, while the temporal variations in the Beaufort Sea show agreement levels comparable to mainstream reanalysis products (Fig. 7d–e; Hall et al., 2021).

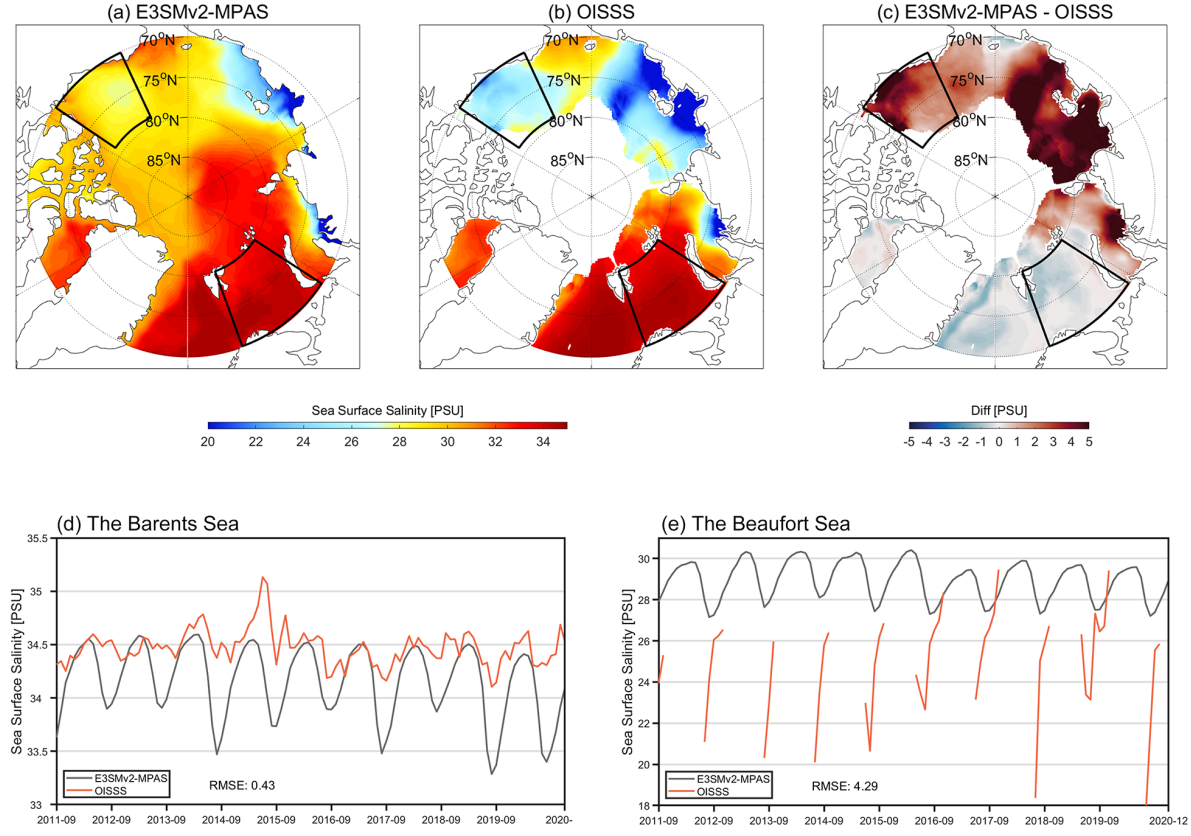

Figure 7. (a–b) September 2011–December 2020 climatological mean sea surface salinity (SSS) spatial distributions: (a) E3SMv2-MPAS, (b) OISSS. (c) SSS bias field: E3SMv2-MPAS vs. OISSS. (d–e) Regional SSS time series in (d) the Barents Sea and (e) the Beaufort Sea (black boxes in a–c; E3SMv2-MPAS: black; OISSS: red).

In the Greenland and Barents Seas, systematic underestimation of SST and SSS (Figs. 6a–c, 7a–c) coincides with overestimation of SIC (Fig. 3a–g). Three-dimensional thermohaline profile analysis (1995–2014, with WOA23, figure omitted) reveals satisfactory mid-depth salinity simulations but overestimation of temperature in the Barents Sea subsurface layers. This indicates effective capture of AW inflow (characterized by high temperature and salinity) through the Barents

https://doi.org/10.5194/egusphere-2025-2665
Preprint. Discussion started: 10 July 2025

Sea Opening (BSO), albeit with slight thermal influence overestimation. Surface thermohaline underestimation may originate from insufficient representation of subsurface-to-surface vertical mixing processes: reduced surface heat/salt fluxes caused by underestimated mixing efficiency could enhance sea ice maintenance mechanisms, thereby amplifying overestimation of SIC. These vertical process biases, combined with surface freshwater transport limitations, constitute key uncertainty sources in regional climate simulations.

3.3 Three-Dimensional Thermohaline Structure

Accurate simulation of three-dimensional thermohaline fields remains a core technical challenge in ocean model development, directly determining model capability in representing Arctic multi-sphere coupling processes (ocean-ice-atmosphere). While preliminary evaluations of sea ice thickness-concentration and surface thermohaline diagnostics have validated E3SMv2-MPAS's capacity to simulate Arctic shallow-layer thermal states, subsurface-to-deep thermohaline structure biases may still induce circulation distortions, material transport deviations, cross-basin exchange inaccuracies, and climate feedback misrepresentations. A multi-dimensional verification framework including spatial heterogeneity diagnostics, temporal evolution analysis and three-dimensional dynamical validation is established to assess E3SMv2-MPAS's three-dimensional thermohaline simulation performance comprehensively.

Using the 1995–2014 climatological mean profiles, systematic comparisons are conducted between E3SMv2-MPAS, observational data (Muilwijk et al., 2023), and 13 high-resolution CMIP6 models (horizontal resolution <60 km; Muilwijk et al., 2023; see Table 1) across four regions: the western Eurasian Basin, the eastern Eurasian Basin, the Chukchi Sea, and the Beaufort Sea. Thermohaline profile characteristics (0–1000 m depth) are evaluated through vertical structure evolution and regional variability analyzes.

Although the CMIP6 models have relative high-resolution, they exhibit systematic biases in AW core characterization as follows: (1) Substantial underestimation of core temperatures (e.g., <0°C in CanESM5 and GISS-E2-1-H), and (2) Overestimated AW layer thickness with obviously downward-shifted core depths. These challenges are particularly pronounced in the western Eurasian Basin influenced by the Fram Strait branch (one of two primary AW inflow pathways) compared to the eastern Eurasian Basin and the Amerasian Basin sector. Observational data reveal maximum temperatures (1.5°C) at 250 m depth in the western Eurasian Basin, decreasing to 0°C at 800 m (Fig. 8a). However, all CMIP6 models show structural biases with temperature maxima averaging 500 m depth and underestimated vertical temperature gradients. In contrast, E3SMv2-MPAS can successfully reproduces observed vertical temperature structure, matching the observed 250 m temperature maximum depth and maintaining temperature decline to 0°C at 1000 m depth. Despite a 1°C core temperature overestimation and 200 m layer thickness bias, its temperature profile RMSE (0.448) significantly outperforms other CMIP6 models.

https://doi.org/10.5194/egusphere-2025-2665
Preprint. Discussion started: 10 July 2025

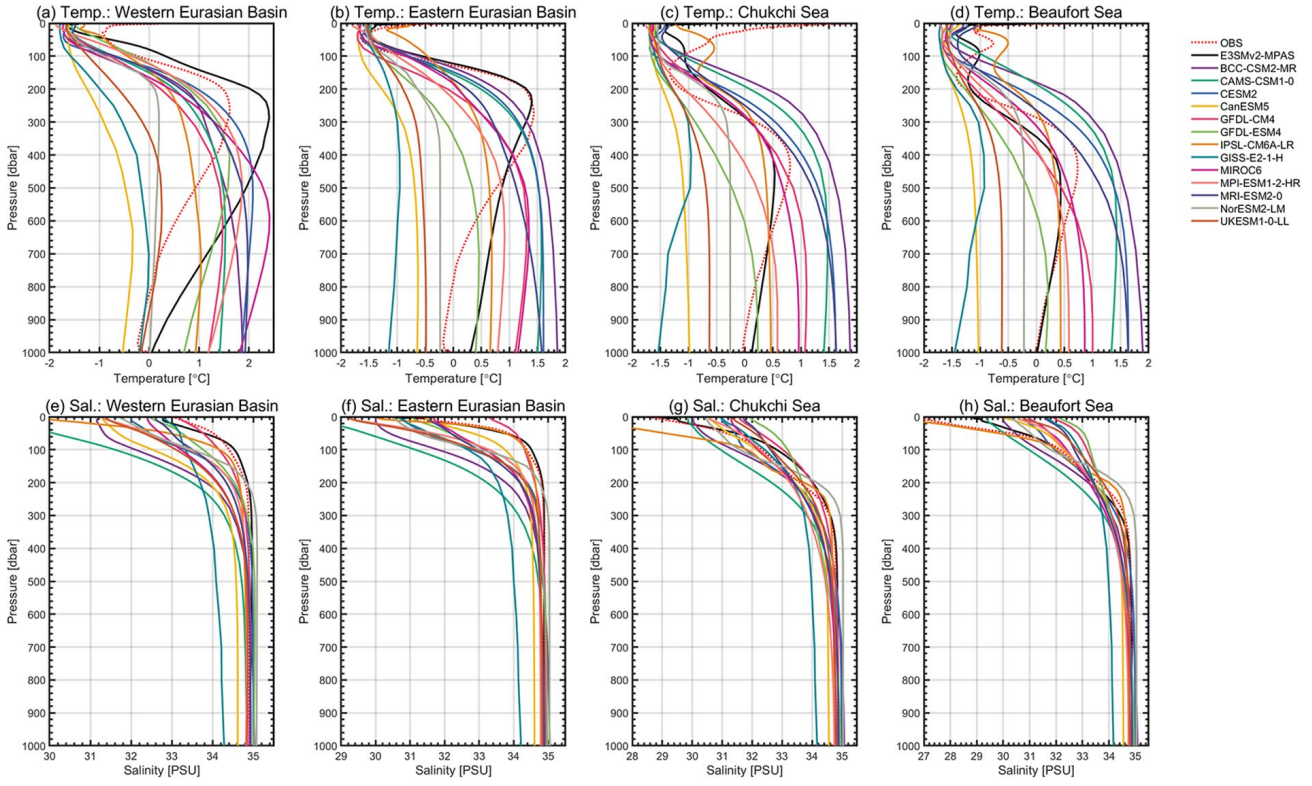

Figure 8. (a–d) 1995–2014 climatological mean temperature profiles from observations (Muilwijk et al., 2023), E3SMv2-MPAS, and the 13 models of CMIP6 (Muilwijk et al., 2023). (e–h) The same as panels (a–d) but for salinity profiles. Basins: the Western Eurasian (a/e), the Eastern Eurasian (b/f), the Chukchi Sea (c/g), the Beaufort Sea (d/h).

Observational spatial heterogeneity shows progressive temperature core reductions (1.6°C→1.4°C→0.7°C→0.6°C) and deepening core depths (250 m→290 m→400 m→420 m) from the western Eurasian Basin to the Beaufort Sea (Fig. 8a–d). CMIP6 models fail to capture these spatial gradients, exhibiting homogeneous vertical structures. E3SMv2-MPAS maintains systematic temperature overestimation (~0.5°C average) while successfully reproducing spatiotemporal evolution of vertical thermal structures. In salinity simulations, systematic underestimation is observed across CMIP6 models within the upper 500 m (Fig. 8e–h). E3SMv2-MPAS demonstrates optimal salinity profile fitting capability through observational agreement starting from 200 m depth, as evidenced by the western Eurasian Basin RMSE of 0.204.

Regional evaluations confirm E3SMv2-MPAS's optimal performance across key metrics: the western Eurasian Basin (temperature RMSE=0.448, salinity RMSE=0.204; Table 2), the eastern Eurasian Basin (0.344, 0.356), the Chukchi Sea (0.686, 0.302), and the Beaufort Sea (0.349, 0.811). Notably, IPSL-CM6A-LR marginally outperforms E3SMv2-MPAS in the eastern Eurasian Basin and the Beaufort Sea salinity simulations, primarily due to surface salinity overestimation in E3SMv2-MPAS.

https://doi.org/10.5194/egusphere-2025-2665
Preprint. Discussion started: 10 July 2025

Table 2. Root mean square errors (RMSE) for temperature (Temp.; °C) and salinity (Sal.; PSU) in 0–1000 m vertical profiles from E3SMv2-MPAS and 13 CMIP6 models (Muilwijk et al., 2023), evaluated against observation (Muilwijk et al., 2023) in four regions: the Western Eurasian Basin, the Eastern Eurasian Basin, the Chukchi Sea, and the Beaufort Sea. Performance ranking: * indicates lowest RMSE per basin/variable, underlined values denote second-lowest.

	Western Eurasian Basin		Eastern Eurasian Basin		Chukchi Sea		Beaufort Sea	
	Temp.	Sal.	Temp.	Sal.	Temp.	Sal.	Temp.	Sal.
E3SMv2-MPAS	0.448*	0.204*	0.344*	0.356	0.686*	0.302*	0.349*	0.811
BCC-CSM2-MR	0.742	1.711	0.700	1.842	1.088	0.784	0.996	0.922
CAMS-CSM1-0	0.692	2.276	0.635	2.263	0.913	1.094	0.916	1.007
CESM2	0.804	0.717	0.672	1.027	0.784	0.635	0.760	0.958
CanESM5	1.497	1.389	1.317	0.698	1.254	0.739	1.047	1.307
GFDL-CM4	0.875	0.296	0.903	1.226	0.941	1.206	0.730	2.135
GFDL-ESM4	0.641	0.449	0.827	0.787	1.011	1.389	0.705	2.195
IPSL-CM6A-LR	0.620	1.389	0.584	0.256*	0.830	1.873	0.485	0.562*
GISS-E2-1-H	1.320	0.795	1.365	1.119	1.381	1.075	1.183	1.946
MIROC6	1.070	0.790	0.780	0.890	0.905	1.054	0.606	1.642
MPI-ESM1-2-HR	0.795	0.856	0.687	1.200	0.833	0.693	0.564	1.309
MRI-ESM2-0	0.839	0.556	0.768	0.930	0.913	1.198	0.701	1.817
NorESM2-LM	0.745	0.819	0.904	1.040	0.884	0.694	0.625	1.220
UKESM1-0-LL	1.022	1.134	1.102	1.076	1.278	1.444	0.883	2.122

Comprehensive analysis of higher-resolution CMIP6 models reveals common thermohaline simulation biases (Fig. 8). To evaluate resolution sensitivity in Arctic Intermediate Water simulations, the assessment framework is extended to five resolution-matched model pairs from OMIP2 (Wang et al., 2024; see Table 1). Thermohaline profile characteristics in the Eurasian and Amerasian Basins are systematically compared between high/low-resolution model pairs (solid/dashed lines), E3SMv2-MPAS, and WOA23 data (Locarnini et al., 2024; Reagan et al., 2024) to elucidate ocean model grid configuration impacts (Fig. 9). Low-resolution models exhibit persistent CMIP6 systematic biases, while their high-resolution counterparts (excluding IAP-LICOM-6.8km) demonstrate improved intermediate water core temperature and vertical structure simulations. High-resolution models successfully reproduce observed zonal gradients showing temperature maxima decreasing from the Eurasian Basin (1.3°C@250 m) to the Amerasian Basin (0.7°C@400 m), confirming resolution enhancement benefits for oceanic frontal processes. In the Eurasian Basin where simulation biases are most pronounced, the

https://doi.org/10.5194/egusphere-2025-2665
Preprint. Discussion started: 10 July 2025

majority of high-resolution models – with the exception of E3SMv2-MPAS (10 km) and FESOM variants (4.5/24 km) – continue to exhibit overestimated AW layer thickness. WOA23 observations indicate temperature decline to 0°C at 800 m depth, whereas most models maintain ~0.5°C at 1000 m (Fig. 9a). This persistent discrepancy demonstrates that resolution enhancement alone remains insufficient to fully resolve key technical bottlenecks in Arctic Intermediate Water simulations. Notably, E3SMv2-MPAS and FESOM models exhibit breakthrough performance (Table 3). Despite comparable resolutions to other high-resolution models (e.g., ACCESS-MOM 9 km, FSU-HYCOM 32 km), unstructured mesh configurations enable refined representation of key hydrographic gateways like the Fram Strait. Compared to tripolar grid models suffering numerical dissipation near complex coastlines, variable mesh designs achieve reduced the Eurasian Basin temperature errors under equivalent computational resources. Model grid type and computational efficiency exhibit nonlinear relationships. Unstructured meshes (FESOM/MPAS) permit dynamic optimization through localized refinement in critical regions (e.g., AW intrusion pathways). This targeted refinement strategy provides new technical approaches for Arctic ocean modeling, particularly under accelerating Atlantification processes.

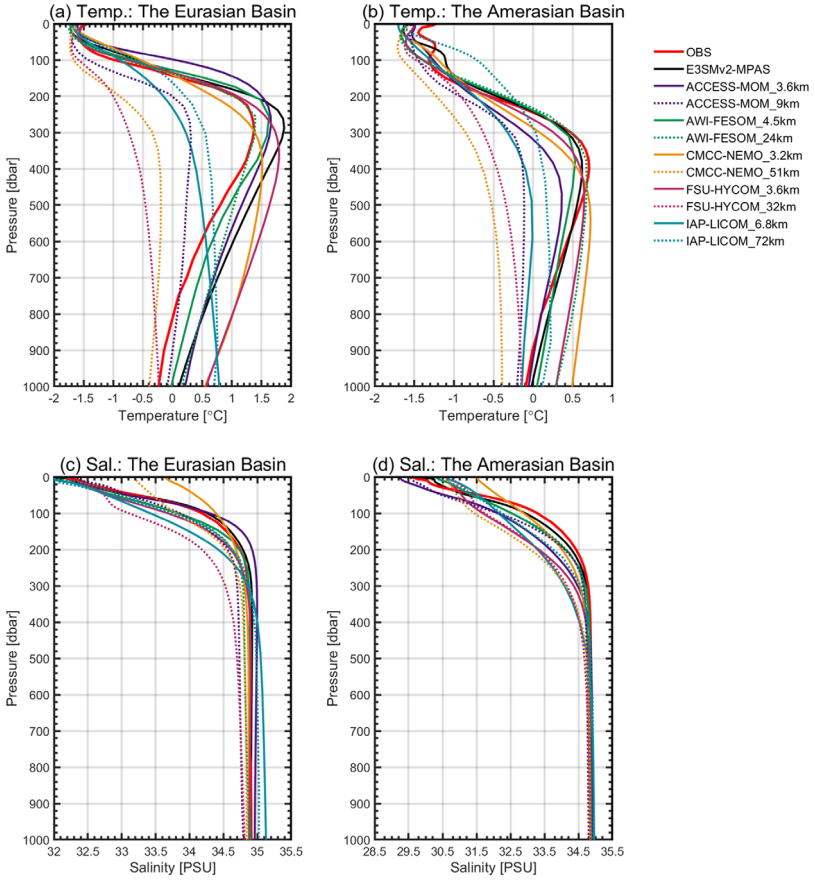

Figure 9. (a–b) 1995–2014 climatological mean temperature profiles in (a) the Eurasian Basin and (b) the Amerasian Basin: Observations (WOA23; red), E3SMv2-MPAS (black), OMIP2 models (Wang et al., 2024; dashed: low-resolution, solid: high-resolution). (c–d) The same as panels (a–b) but for salinity profiles.

https://doi.org/10.5194/egusphere-2025-2665
Preprint. Discussion started: 10 July 2025

Table 3. Root mean square errors (RMSE) for temperature (Temp.; °C) and salinity (Sal.; PSU) in 0–1000 m vertical profiles from E3SMv2-MPAS and 5 OMIP2 model pairs (Wang et al., 2024), evaluated against WOA23 in the Eurasian Basin and the Amerasian Basin. Performance ranking: * indicates lowest RMSE per basin/variable, underlined values denote second-lowest.

	Eurasian Basin		Amerasian Basin	
	Temp.	**Sal.**	**Temp.**	**Sal.**
E3SMv2-MPAS	0.223*	0.130*	0.143*	0.219*
ACCESS-MOM_3.6km	0.437	0.202	0.217	0.663
ACCESS-MOM_9km	0.583	0.208	0.423	0.557
AWI-FESOM_4.5km	0.236	0.205	0.207	<u>0.390</u>
AWI-FESOM_24km	<u>0.230</u>	<u>0.187</u>	0.253	0.397
CMCC-NEMO_3.2km	0.453	0.762	0.276	1.055
CMCC-NEMO_51km	0.869	0.600	0.558	0.875
FSU-HYCOM_3.6km	0.409	0.240	<u>0.186</u>	0.719
FSU-HYCOM_32km	1.012	0.442	0.485	0.797
IAP-LICOM_6.8km	0.716	0.457	0.346	0.882
IAP-LICOM_72km	0.435	0.319	0.456	0.716

Following systematic benchmarking against CMIP6/OMIP2 multi-resolution models, we investigate parameterization sensitivity within the same coupled framework (E3SM). By comparing mesoscale eddy parameterization schemes between E3SMv1 and v2 (as detailed in Section 2.2.3), we dissect their impacts on simulation fidelity and elucidate underlying mechanism. Comparative assessments of E3SM-Arctic-OSI (E3SMv1; Veneziani et al., 2022) and E3SMv2-MPAS (both 60to10 km) are performed across the Eurasian Basin, the Amerasian Basin, and sub-regions (Fig. 10). E3SMv2-MPAS demonstrates improved temperature vertical structure simulations (Fig. 10a–f), reducing Eurasian Basin core temperature overestimation from 1.3°C to 0.5°C and correcting 100 m core depth shoaling. Optimized mesoscale transport parameterization better represents turbulent mixing effects on water mass structure. For salinity, E3SM-Arctic-OSI exhibits -0.7 PSU biases above 200 m in the Eurasian Basin, reduced to -0.13 PSU in E3SMv2-MPAS (Fig. 10g). This enhancement likely stems from the refined vertical mixing scheme in E3SMv2-MPAS, which better captures Arctic halocline dynamics. Notably, E3SM-Arctic-OSI outperforms E3SMv2-MPAS in simulating sub-maximum temperature gradients (500–1000 m layer), with the Eurasian Basin RMSE reduced by 65% (0.17 vs. 0.49 in v2). This regression is attributed to excessive subsurface gradient smoothing in E3SMv2-MPAS caused by persistent moderate diffusion at 10 km Arctic resolution.

https://doi.org/10.5194/egusphere-2025-2665
Preprint. Discussion started: 10 July 2025

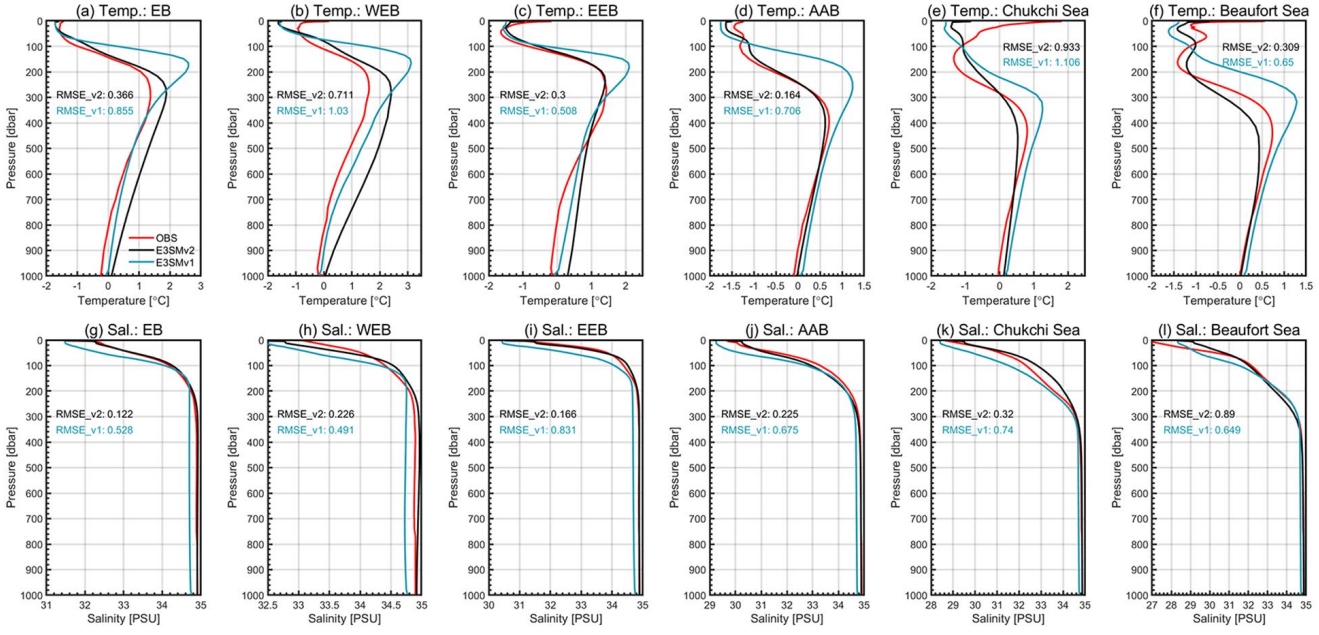

Figure 10. (a–f) 2005–2014 climatological mean temperature profiles: Observations (WOA23 for EB/AAB; observation from Muilwijk et al., 2023 for WEB/EEB/Chukchi/Beaufort; red lines), E3SMv2-MPAS (black lines), E3SM-Arctic-OSI (Veneziani et al., 2022; blue lines). (g–l) The same as panels (a–f) but for salinity profiles. Basins: the Eurasian Basin (EB, a/g), the Western Eurasian Basin (WEB, b/h), the Eastern Eurasian Basin (EEB, c/i), the Amerasian Basin (AAB, d/j), the Chukchi Sea (e/k), the Beaufort Sea (f/l).

Physical parameterization upgrades and resolution enhancement demonstrate synergistic effects. E3SMv2-MPAS addresses CMIP6/OMIP2 intermediate water simulation challenges through improved subgrid parameterization and the inherent advantages of unstructured meshes. The fundamental limitation of traditional eddy parameterization in variable-resolution meshes is revealed: complete GM deactivation (κ=0) causes structural distortions, while moderate diffusion (κ=300 $m^2\ s^{-1}$) induces over-smoothing. FESOM_4.5km's superior temperature-depth relationships suggest potential solutions through MPAS resolution increases or parameterization optimization via neural networks. Opposing regional biases (Eurasian overestimation/Amerasian underestimation) indicate current parameterizations lack universality across Arctic dynamical regimes, highlighting critical development pathways for next-generation models.

In order to systematically assess model capabilities in representing multi-scale Arctic thermal variations, an inter-decadal three-dimensional thermohaline evolution framework is established. Depth-time section comparisons between E3SMv2-MPAS and EN.4.2.2 (Good et al., 2013) are conducted to analyze spatiotemporal heterogeneity in Arctic oceanic thermal structures (Fig. 11).

https://doi.org/10.5194/egusphere-2025-2665
Preprint. Discussion started: 10 July 2025

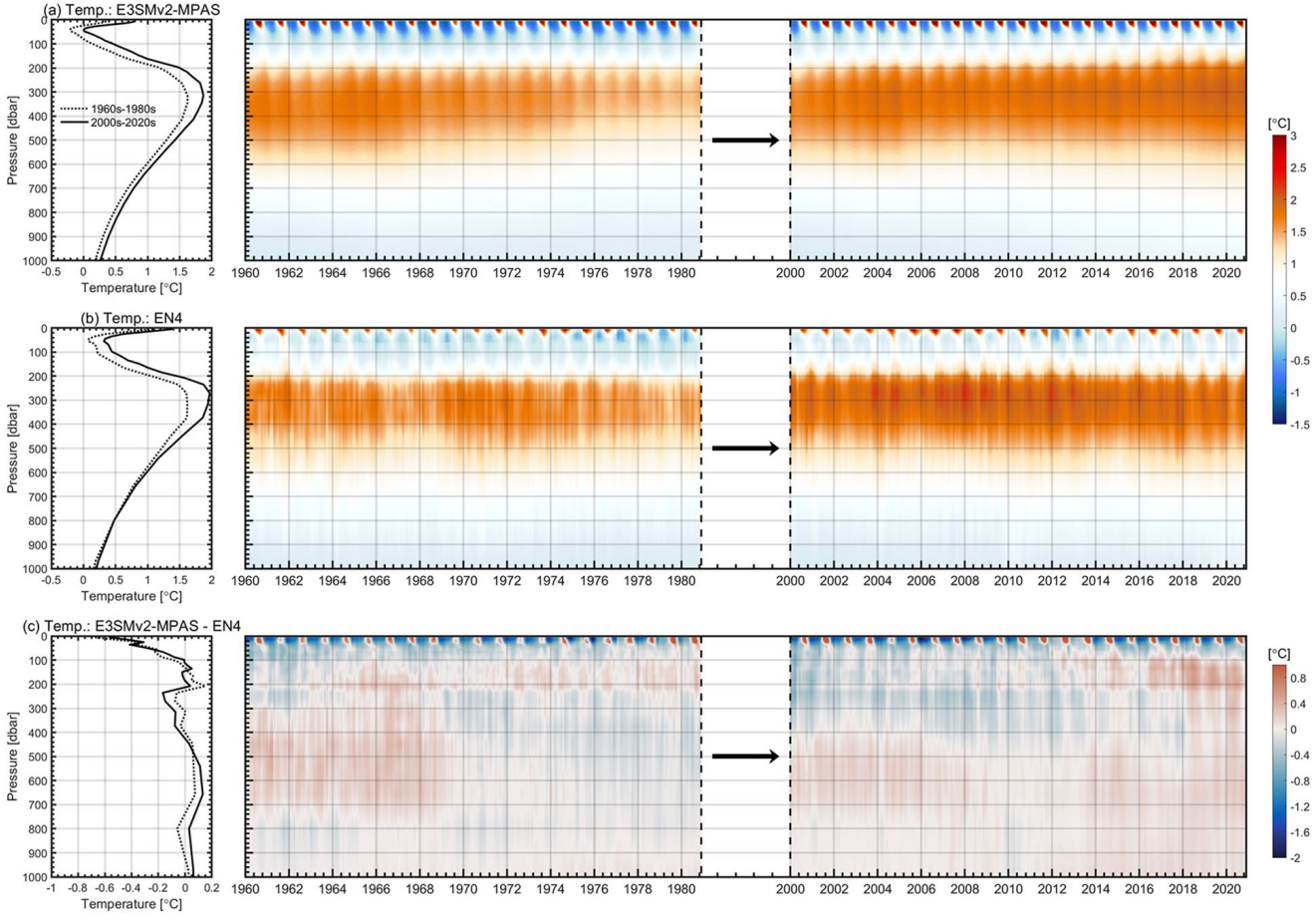

Figure 11. (a) E3SMv2-MPAS simulated temperature profiles (0–1000 m): 1960–1980 climatology (dashed) vs. 2000–2020 climatology (solid). Right: Hovmöller diagram of depth-time evolution (1960–1980 and 2000–2020). (b) The same as panel (a) but for EN.4.2.2. (c) The same as panel (a) but for E3SMv2-MPAS minus EN.4.2.2 differences.

E3SMv2-MPAS successfully reproduces the solar radiation-driven seasonal thermal cycle observed in EN.4.2.2 (Fig. 11). Monthly thermohaline profiles (depth-month coordinates) in the upper 500 m of the Eurasian Basin better illustrate radiation-dominated seasonal characteristics: summer (June–August) surface temperature peaks coincide with salinity minima from meltwater inputs, while winter (December–February) shows sub-freezing temperatures (<-1.8°C) and salinity recovery (Fig. 12). These core seasonal features are accurately captured, validating high-precision surface flux representation.

https://doi.org/10.5194/egusphere-2025-2665
Preprint. Discussion started: 10 July 2025

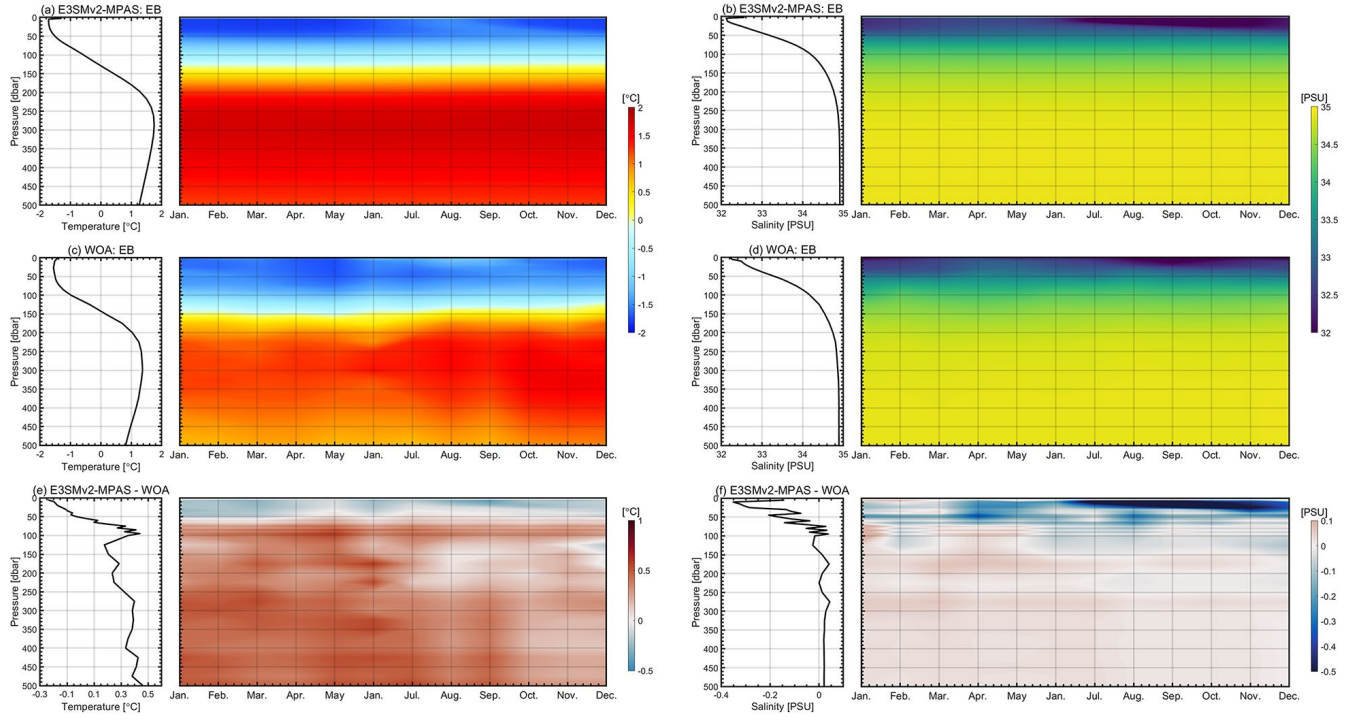

Figure 12. (a–b) E3SMv2-MPAS simulated 1995–2020 climatological mean (left) temperature and (right) salinity profiles (0–500 m) in the Eurasian Basin, with Hovmöller diagrams of monthly variability. (c–d) The same as panels (a–b) but for WOA23. (e–f) The same as panels (a–b) but for model-observation differences (E3SMv2-MPAS minus WOA23).

E3SMv2-MPAS demonstrates exceptional multi-temporal simulation capabilities for AW dynamics (Fig. 11). Observations reveal stable AW core temperatures (~1.6°C) during 1960–1980, increasing to ~2°C in 2000–2020 with core shallowing from 350 m to 300 m (Fig. 11b). E3SMv2-MPAS accurately reproduces both the ~0.4°C warming magnitude and ~50 m vertical migration (Fig. 11a). However, regional-specific biases emerge in seasonal variability simulations (Fig. 12). EN.4.2.2 identifies semi-annual signals in the 200–500 m layer of the Eurasian Basin (September–November peaks at ~1.5°C; Fig. 12c), linked to winter Atlantification intensification. E3SMv2-MPAS fails to capture this seasonality, producing persistent warm biases in 200–400 m layers with overestimated spring–summer core temperatures (0.5–0.8°C; Fig. 12e).

A systematic validation framework uncovers the multi-tiered optimization characteristics of E3SMv2-MPAS, demonstrating superior surface-layer accuracy alongside relatively excellent intermediate-depth representations. Nevertheless, inherent constraints of current parameterization schemes under polar stratification conditions lead to persistent model-data discrepancies, particularly manifested in seasonal phase mismatches. This finding highlights the need to develop improved turbulence models based on energy transfer principles (Canuto et al., 2001; Smagorinsky, 1963), which would better connect processes across different scales.

We further investigate the decadal-scale thermohaline variability across Arctic basins. The results reveal regional heterogeneity in temperature and salinity trends (Fig. 13), likely modulated by differential ocean-ice feedbacks and cross-

https://doi.org/10.5194/egusphere-2025-2665
Preprint. Discussion started: 10 July 2025

basin transport dynamics. Inter-decadal comparisons (1970s vs. 2000s–2020s; Muilwijk et al., 2023) reveal pan-Arctic synchronous warming across the Eurasian Basin sectors and the Amerasian sub-regions (Fig. 13e–h). However, E3SMv2-MPAS underestimates the warming in the Amerasian Basin (0.1–0.5°C biases; Fig. 13c–d and g–h), indicating limitations in AW transport pathways and heat redistribution.

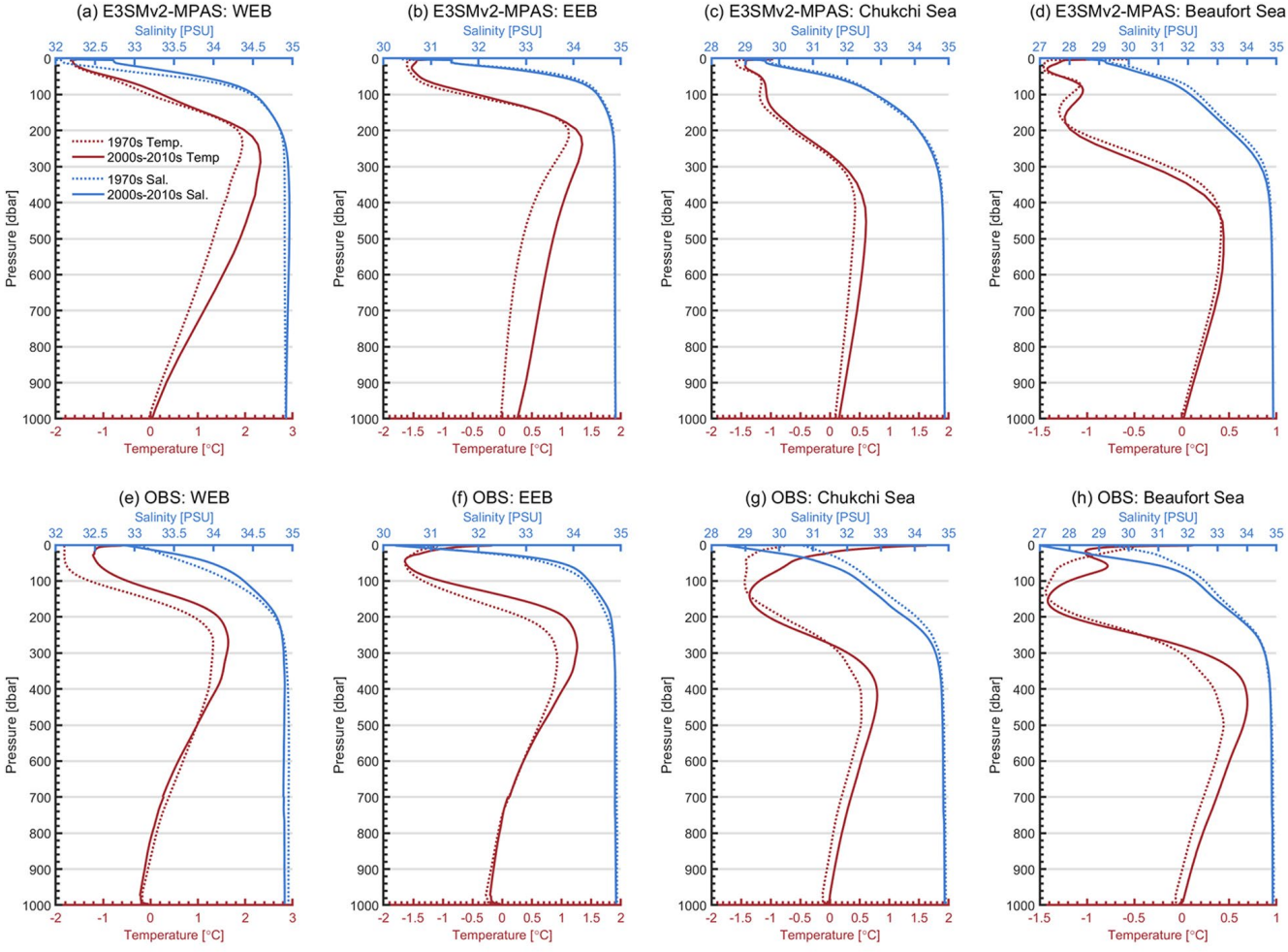

Figure 13. (a–d) Vertical profiles of climatological mean temperature (red curves) and salinity (blue curves) in the Western Eurasian Basin (WEB, a), the Eastern Eurasian Basin (EEB, b), the Chukchi Sea (c), and the Beaufort Gyre (d) from E3SMv2-MPAS: dashed lines denote 1970s (1971–1979), solid lines represent 2000s–2010s (2001–2019). (e–f) Corresponding observational profiles from Muilwijk et al., (2023) with identical temporal averaging.

In the Eurasian Basin upper layers (~100–450 m; Fig. 13a–b and e–f), observations show dual-mode thermal evolution: shallow warming above temperature cores (100–250 m) contrasts with systematic warming below (250–450 m). Model simulations exhibit spatial heterogeneity: 0.2±0.1°C underestimation of shallow warming contrasts with excessive vertical response ranges (250–1000 m vs. observed 250–450 m). Notably, simulated AW layer thickening in the eastern Eurasian Basin during 2000s–2010s lacks observational support (Fig. 13b and f).

https://doi.org/10.5194/egusphere-2025-2665
Preprint. Discussion started: 10 July 2025

In the Amerasian Basin side, observations indicate basin-wide warming from core layers to AW bottom (~1000 m), with the Chukchi Sea showing ΔT=0.2±0.1°C (Fig. 13c–d and g–h). While successfully reproducing Chukchi thermal trends, E3SMv2-MPAS exhibits systematic Beaufort Sea deviations. Salinity changes primarily occur in the upper 300 m of the Amerasian Basin (observed ΔS=-0.3±0.2 PSU), with the model failures in capturing the freshening of the Chukchi Sea and underestimation of trends in the shallow-layer (<80 m) of the Beaufort Sea.

E3SMv2-MPAS demonstrates significant regional dependence in simulating interdecadal thermohaline structure changes across Arctic basins. Systematic biases persist between model outputs and observational data, particularly in AW layer thickness evolution, vertical extent of subsurface warming processes, and strength of surface freshening signals. These discrepancies likely originate from suboptimal parameterization schemes for key physical processes such as mesoscale eddy activities and shelf-basin interactions.

AW demonstrates systematic cooling and freshening (temperature and salinity reduction) during its transport from the Eurasian to the Amerasian Basin (Fig. 8), a transformation likely modulated by baroclinic adjustment processes in the inter-basin transition zone. These processes, known to govern cross-basin material-energy exchange (Aksenov et al., 2016), necessitate a three-dimensional thermohaline diagnostic approach. To this end, we analyze coordinated meridional sections along 145°W (the Amerasian Basin) and 70°E (the Eurasian Basin), constructing a unified framework to evaluate spatiotemporal variability in AW properties (Fig. 14). WOA23-based comparisons confirm E3SMv2-MPAS's capability in reproducing inter-basin gradient characteristics through three key aspects: (1) AW thermal attenuation: Successful simulation of core temperature decreases from the Eurasian to the Amerasian Basin, replicating thermodynamic dissipation processes; (2) Stratification depth displacement: Realistic representation of westward-decreasing upper boundary depths matching slope current adjustments; (3) Surface freshwater transport effects: Accurate reproduction of the surface salinity depression in the Amerasian Basin relative to the Eurasian Basin, validating appropriate parameterization of Pacific-origin freshwater influx mechanisms. Persistent thermal biases in the Eurasian Basin emerge in 145°W sections, with maximum +2°C warm deviations in 100–500 m core layers (Fig. 14e). These discrepancies may originate from overestimation of the Fram Strait heat fluxes or inadequate parameterization of mesoscale mixing. Despite absolute temperature biases, maintained meridional heat transport gradients confirm fundamental physical framework validity for large-scale advection processes.

https://doi.org/10.5194/egusphere-2025-2665
Preprint. Discussion started: 10 July 2025

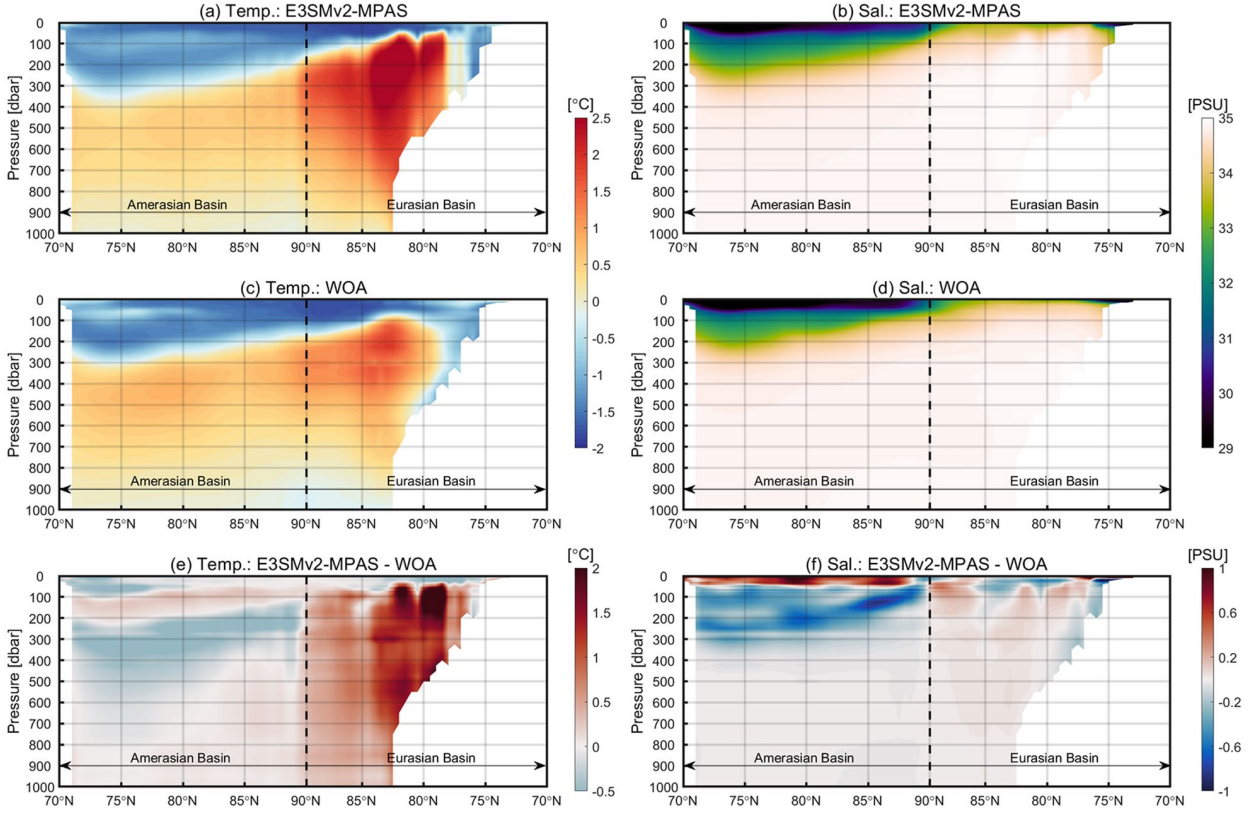

Figure 14. (a–b) E3SMv2-MPAS simulated 1995–2020 climatological (left) temperature and (right) salinity distributions along the 145°W–70°E transect (location mapped in Fig. 1b). (c–d) The same as panels (a–b) but for WOA23. (e–f) The same as panels (a–b) but for the model-observation differences (E3SMv2-MPAS minus WOA23).

4 Atlantic Water Layer States

4.1 Parametric Characterization of Atlantic Water Core

As demonstrated in Section 3, model biases predominantly manifest in two critical parameters: AW core temperature (AWCT) and depth (AWCD). These metrics, defined as the maximum temperature within 150–900 m depth and its corresponding depth (Khosravi et al., 2022; Shu et al., 2022; Wang et al., 2024), are employed to evaluate E3SMv2-MPAS's performance in reproducing spatiotemporal features of AW (Fig. 15). Observational AWCT/AWCD datasets from Richards et al., (2022) reveal successful model reproduction of baseline spatial gradients: decreasing AWCT and increasing AWCD from the Eurasian to the Amerasian Basin, though with marked regional heterogeneity (Fig. 15a–d). Systematic overestimation of AWCT (+0.5°C) is identified in the western Eurasian Basin off-shelf regions (high-latitude sectors), potentially linked to biased inflow heat flux allocation in the Fram Strait. Similar positive deviations (+0.5°C) in the Beaufort Sea maybe suggest inadequate Pacific inflow mixing parameterization. AWCD simulations demonstrate higher accuracy, with minor underestimation (ΔZ<100 m) in the eastern Eurasian Basin.

https://doi.org/10.5194/egusphere-2025-2665
Preprint. Discussion started: 10 July 2025

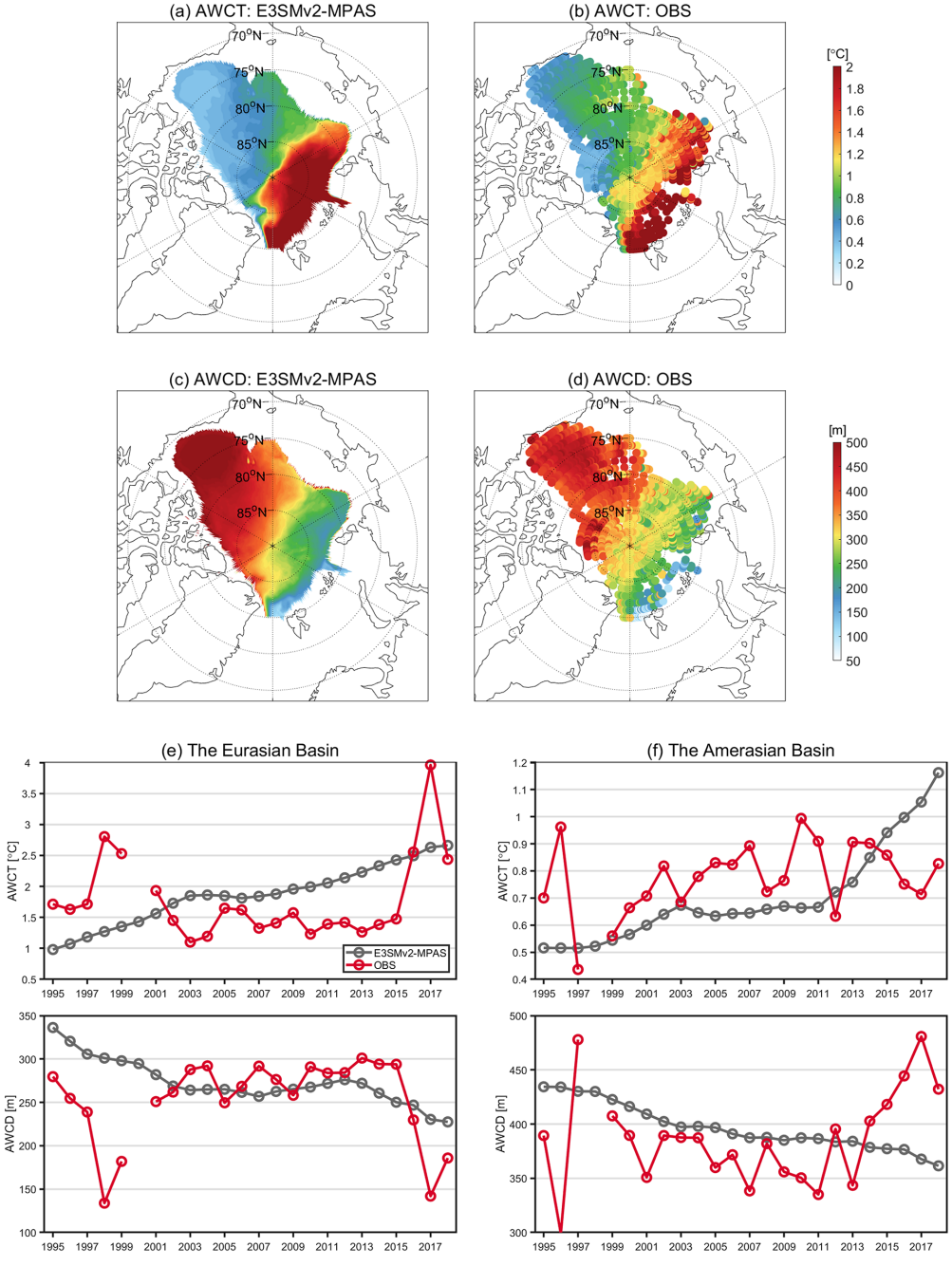

Figure 15. (a–b) 1995–2018 climatological mean Atlantic Water Core Temperature (AWCT) spatial distributions: (a) E3SMv2-MPAS vs. (b) observation from Richards et al., (2022). (c–d) The same as panels (a–b) but for Atlantic Water Core Depth (AWCD). (e–f) Temporal evolution of basin-averaged AWCT (top row) and AWCD (bottom row) in the Eurasian Basin (e) and the Amerasian Basin (f): E3SMv2-MPAS (black) versus observations (red).

https://doi.org/10.5194/egusphere-2025-2665
Preprint. Discussion started: 10 July 2025

Interannual variability (1995–2018) is adequately captured through basin-averaged AWCT/AWCD magnitudes (Fig. 15e–f). E3SMv2-MPAS successfully reproduces AWCT warming trends in both basins, AWCD shoaling in the Eurasian Basin, and 1995–2013 AWCD declines in the Amerasian Basin. However, post-2013 increases in AWCD in the Amerasian Basin remain unresolved. While demonstrating credibility in long-term trend simulations, model responsiveness to decadal-scale climatic shifts requires boundary condition dynamization and mixing process optimization – critical for predicting nonlinear Atlantification trajectories.

Cross-validation under the OMIP2 framework (Wang et al., 2024) reveals that among five resolution-varied model groups, only FESOM_4.5km, MOM_3.6km, and HYCOM_3.6km demonstrate high AWCT spatial pattern simulation skills (Fig. 16). FESOM_4.5km outperforms E3SMv2-MPAS (10 km) in representing the western Eurasian Basin shelf-basin gradients, but underperforms in the Amerasian Basin (Fig. 16b–c). Low-resolution models exhibit a systematic underestimation of AWCT, with FESOM_24km being the exception, reaffirming unstructured meshes' polar ocean modeling advantages (Fig. 16h–l).

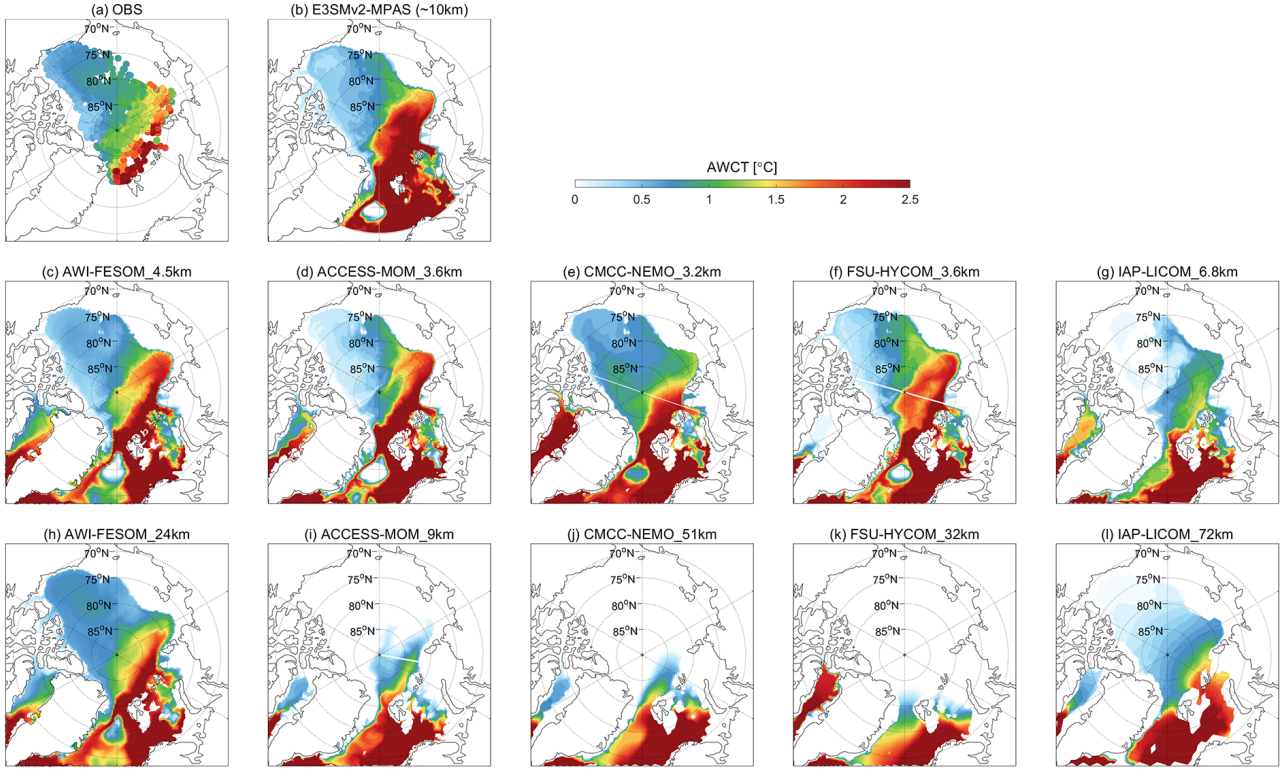

Figure 16. 1995–2018 climatological mean Atlantic Water Core Temperature (AWCT) spatial patterns from (a) observations (Richards et al., 2022), (b) E3SMv2-MPAS, and (c–l) OMIP2 models (Wang et al., 2024). Middle/bottom rows: High-resolution and corresponding low-resolution model pairs from OMIP2.

https://doi.org/10.5194/egusphere-2025-2665
Preprint. Discussion started: 10 July 2025

To address the systematic underestimation of Atlantification in model simulations (mentioned in Section 1), five key parameters are quantified: AWCT, AWCD, AW upper boundary (0°C isotherm; Meyer et al., 2017), AW layer thickness (between 0°C isotherms), and AW heat content. By analyzing their spatiotemporal response characteristics, this study investigates the trans-decadal evolution of Atlantification.

The AW heat content is calculated as follows (Polyakov et al., 2017):

$$Q = \int_{z_1}^{z_2} \rho_w \, c_p (\theta - \theta_{freezing}) dz,$$

where z_1/z_2 denote layer boundaries, ρ_w seawater density, c_p specific heat of seawater, and $\theta_{freezing}$ freezing temperature.

Both basins exhibit coordinated changes during 1960s–1980s and 2000s–2020s: AWCT increases, AWCD decreases, AW upper boundary shallows, layer thickness expands, and heat content accumulates (Fig. 17). Post-2000s acceleration of these trends shows tight coupling with enhanced Atlantic meridional heat transport under Arctic amplification. E3SMv2-MPAS captures the key thermodynamic signatures of Atlantification (the Eurasian Basin vs. the Amerasian Basins between 2000–2020), aligning closely with observationally derived mechanisms of Atlantic Water intrusion and its climatic impacts (Polyakov et al., 2017): (1) A 1°C gradient in AWCT between the Eurasian and Amerasian Basins, consistent with zonal heat dissipation; (2) A 130-m shallower AWCD in the Eurasian Basin, reflecting intensified vertical mixing due to sea ice loss; (3) Synergistic changes in AW layer thickness and heat content (100 m thinner layer with +4000 MJ·m^{-2} in the Eurasian Basin), confirming advective-diffusive redistribution.

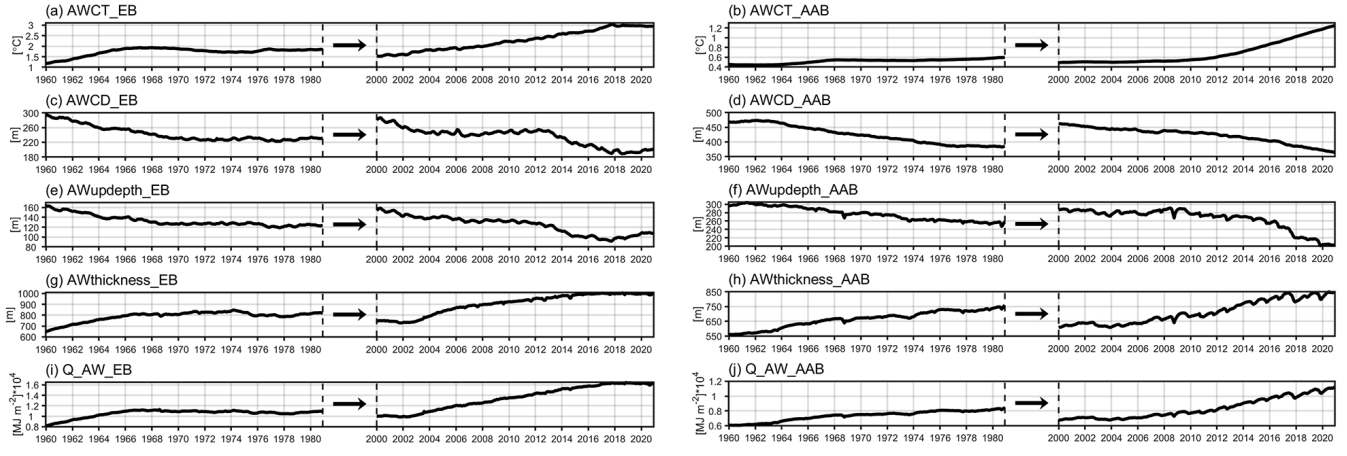

Figure 17. (a–b) 1960–1980 vs. 2000–2020 climatological mean Atlantic Water Core Temperature (AWCT) in the (a) Eurasian and (b) Amerasian Basins. (c–j) The same as panels (a–b) but for Atlantic Water Core depth (AWCD; c–d), Atlantic Water layer upper boundary depth (AWupdepth; e–f), thickness (AWthickness; g–h), and heat content (Q_AW; i–j).

This multi-scale validation confirms E3SMv2-MPAS's physical credibility in reproducing Atlantification mechanisms: cascading heat flux-stratification-heat content responses and inter-basin thermodynamic evolution. The model thus provides critical process fidelity for predicting Arctic oceanic thermal threshold transitions.

https://doi.org/10.5194/egusphere-2025-2665
Preprint. Discussion started: 10 July 2025

4.2 Atlantic Water-Surface Coupling

The AW layer constitutes the most critical oceanic heat reservoir in the Arctic Ocean (Carmack et al., 2015b), containing sufficient thermal energy to melt all Arctic sea ice within several years (Turner, 2010) and capable of dissolving 3–4 times the current ice volume (Carmack et al., 2015a). A pronounced halocline characterized by rapidly increasing salinity with depth typically separates the cold, low-salinity surface waters from the warm, saline AW in the Eurasian and Amerasian Basins. This strong stratification effectively inhibits vertical water mass exchange (Peralta-Ferriz and Woodgate, 2015), isolating the AW layer from sea ice and mixed layer interactions (Aagaard et al., 1981; Richards et al., 2022). Under these physical constraints, vertical heat transport primarily occurs through molecular-scale processes involving internal wave breaking and double-diffusive mixing (Davis et al., 2016). However, since the 1970s, progressive weakening of the eastern Eurasian Basin halocline has been documented (Polyakov et al., 2010; Steele and Boyd, 1998), culminating in its complete failure as an effective thermal barrier for intermediate AW heat by the mid-2010s (Polyakov et al., 2020a). Stratification collapse has triggered a regime shift from double-diffusive dominance to shear-driven turbulent mixing, fundamentally altering vertical heat flux dynamics (Polyakov et al., 2020a).

The KPP scheme employed by E3SMv2-MPAS driven by Gradient Richardson Number (Ri) physics (Zhu et al., 2022). This study evaluates whether this parameterization scheme, combined with the model's unstructured mesh capability, adequately resolves Arctic vertical thermal coupling features, particularly in the Eurasian Basin. A thermal linkage framework is established between the upper (10 m) and intermediate (AW core layer, 400 m) ocean layers to address two critical aspects: (1) spatiotemporal delay characteristics in vertical heat signal propagation relative to AW transport timescales, and (2) potential regime shifts in interlayer coupling mechanisms under climate warming. This diagnostic framework provides dynamic constraints for optimizing vertical mixing parameterizations while elucidating climate impacts of upper-ocean thermal variability.

During 1960–1980 baseline conditions (zero time lag), statistically significant positive correlations ($p<0.05$) between AW layer and surface temperatures are confined to the Norwegian Sea, indicating direct advective heat modulation (Fig. 18a). Lagged correlation analysis reveals basin-scale inertial transport characteristics: localized positive correlations emerge in the Eurasian Basin at 24-month lag, expanding basin-wide by 36 months (Fig. 18b–h). This spatiotemporal inertia is attributed to: (1) Basin-scale recirculation timescales required for AW mass circumpolar transport (e.g., 2-year lag between the Fram Strait and the eastern Eurasian Basin 250 m temperatures; Polyakov et al., 2020b), and (2) efficiency limitations in subsurface mixing processes.

https://doi.org/10.5194/egusphere-2025-2665
Preprint. Discussion started: 10 July 2025

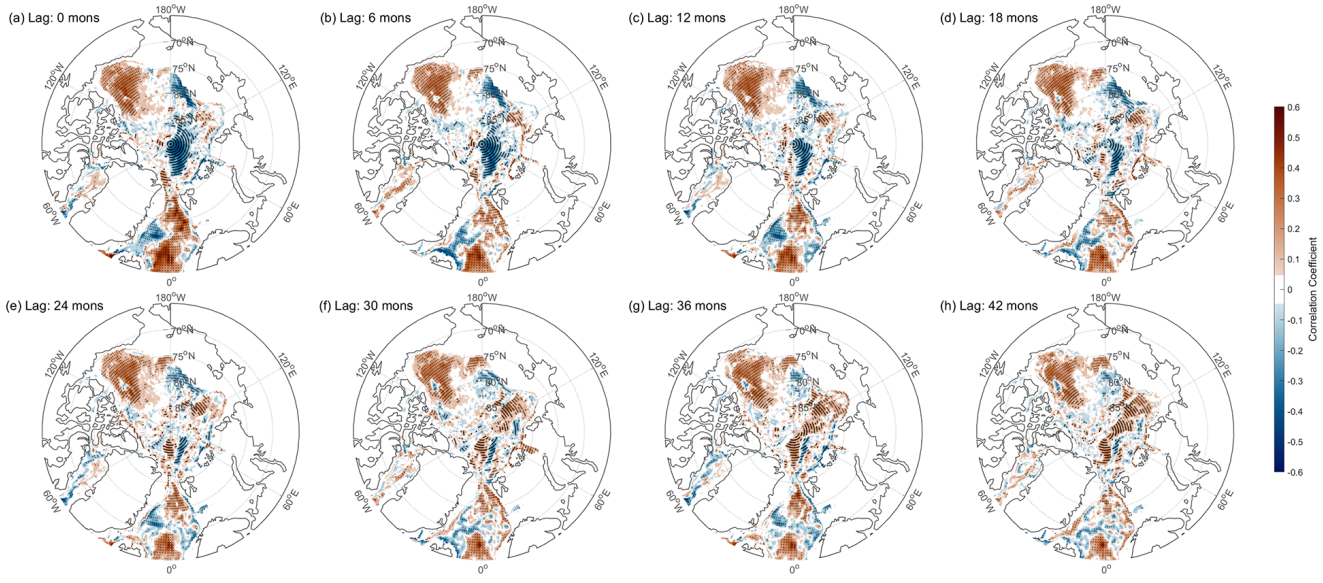

595

Figure 18. (a) 1960–1980 climatological mean correlation between surface (5 m) and mid-depth (400 m) temperatures. (b–h) Lagged correlations at 6-month intervals (lag 6 mons to 42 mons). Black dots indicate significance ($p<0.05$).

The 1995–2020 period exhibits fundamental regime transition: immediate basin-wide positive correlations ($p<0.05$) emerge along AW pathways (from the Fram Strait to the Eurasian Basin) under zero-lag conditions, maintaining stable correlation
600 strength through 42-month lags (Fig. 19). This instantaneous response pattern reflects multiscale Arctic system changes: (1) Increased AWCT with decreased AWCD shortens vertical diffusion pathways, indicating intensified "Atlantification" (Polyakov et al., 2017); (2) Stratification weakening from sea ice loss enhances cross-layer turbulent mixing efficiency (Kwok, 2018; Onarheim et al., 2018; Polyakov et al., 2020a).

https://doi.org/10.5194/egusphere-2025-2665
Preprint. Discussion started: 10 July 2025

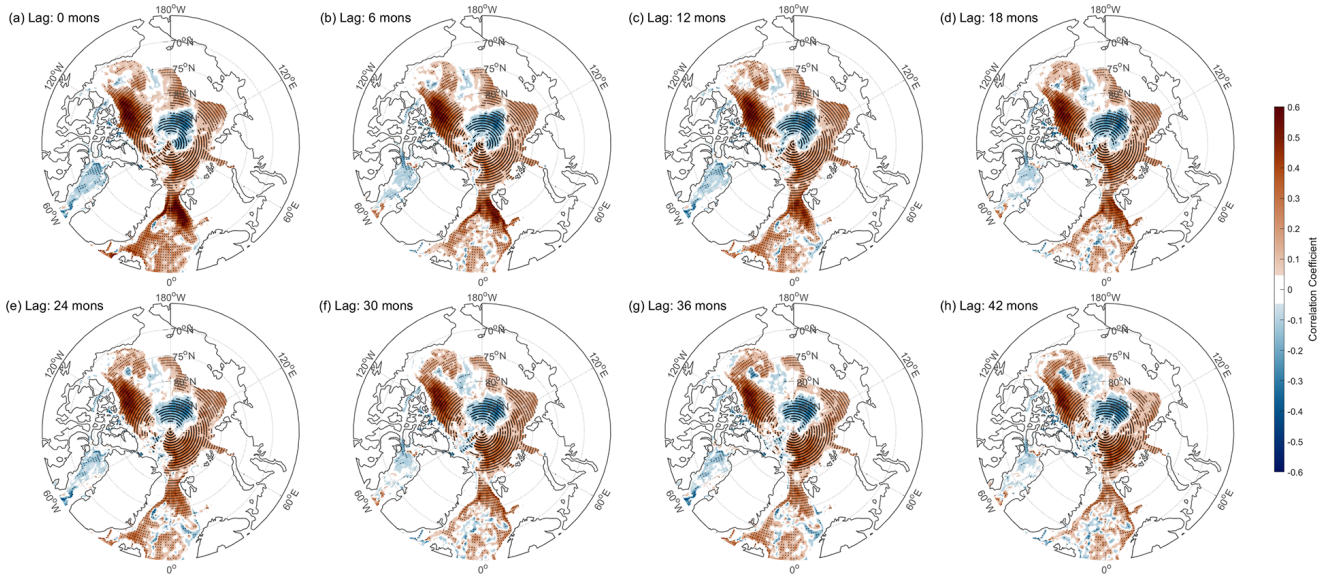

Figure 19. The same as Fig. 18, but for 1995–2020 period.

A fundamental regime shift in Arctic intermediate-to-surface thermal coupling mechanisms under climate warming is revealed through cross-temporal-scale lagged correlation diagnostics: transitioning from historical basin-scale inertial transport patterns to contemporary instantaneous response modes. This regime shift, driven by altered AW thermohaline properties and reduced stratification stability, enhances vertical heat leakage efficiency from intermediate layers. Model evaluation demonstrates that while the KPP scheme captures accelerated heat transport trends, systematic biases persist in nonlinear responses to shear mixing (Figs. 18–19). Future research directions emphasize developing scale-aware parameterizations incorporating high-resolution turbulence observations to improve model capabilities in predicting Arctic energy transport regime shifts.

5 Conclusions

This study systematically evaluates the Arctic ocean-sea ice simulation capabilities of E3SMv2-MPAS through multi-source observations (in situ profiles, satellite remote sensing, optimum interpolation dataests), reanalysis products (NSIDC, HadISST1, ERA5, PIOMAS) and model outputs (CMIP6, OMIP2), with focus on core parameters including sea ice (concentration/thickness; SIC/SIT), surface thermohaline properties (sea surface temperature/salinity; SST/SSS), three-dimensional thermohaline structures, Atlantic Water (AW) heat characteristics, and vertical thermal linkages. Spatial distribution patterns, seasonal-to-decadal variability, and three-dimensional evolutionary processes are comprehensively analyzed.

https://doi.org/10.5194/egusphere-2025-2665
Preprint. Discussion started: 10 July 2025

E3SMv2-MPAS demonstrates significant advantages in Arctic climatology simulations: (1) Accurate representation of spatial heterogeneity and temporal evolution trends in SIC, SIT, and SST (Figs. 3a–g, 4a–c, 6a–c); (2) Superior simulation accuracy for 1995–2020 SIC decline trends compared to Hadley and ERA5 reanalysis products (NSIDC-benchmarked; Fig. 3h); (3) Enhanced SIT reliability in the Greenland Sea and the Canadian Archipelago versus PIOMAS (ICESat-validated; Fig. 5); (4) Consistent SSS spatial patterns and seasonal evolution with leading reanalysis products including HYCOM and GLORYS12 (Fig. 7; Hall et al., 2021).

E3SMv2-MPAS successfully addresses longstanding Arctic simulation biases through synergistic integration of high-resolution Arctic domains, flexible global unstructured meshes, and suitable mesoscale eddy parameterization: (1) Precise reproduction of AW layer thickness/depth and core temperatures (Figs. 8–10, 15–16), achieving minimal RMSE in three-dimensional thermohaline simulations across Arctic basins compared to CMIP6 and OMIP2 models (Tables 1–2); (2) Effective capture of AW warming trends including decadal-scale intermediate layer heating and vertical shoaling of warm cores (Figs. 11, 13); (3) Realistic simulation of accelerated Atlantification processes, evidenced by post-2000 intensification in AW core temperature and heat content while reduced AW core depth, upper boundary and layer thickness, and instantaneous surface-intermediate heat transfer in the Eurasian Basin (Figs. 17–19). Additional breakthroughs include successful representation of solar-driven seasonal upper-ocean thermal cycles (Fig. 12) and inter-basin water mass gradient evolution from the Eurasian Basin to the Amerasian Basin (e.g., AW thermohaline attenuation, vertical stratification shifts, and surface freshwater transport effects; Fig. 14). These advancements establish critical numerical platforms for investigating Arctic stratification destabilization and cross-scale energy transfer mechanisms, particularly for quantifying mesoscale modulation of ocean-sea ice-atmosphere feedbacks.

Notwithstanding these achievements, key limitations persist: (1) Systematic overestimation of SIT in the Canadian Basin (0.5–1 m bias; Fig. 5), potentially linked to misrepresentation of Beaufort Gyre intensity enhancing ice convergence, requiring verification through eddy kinetic energy budget analysis; (2) Coordinated underestimation of SST/SSS and overestimation of SIC in the Greenland and Barent Seas (Figs. 3a–g, 4a–c, 6a–c), attributable to underestimated efficiency of vertical mixing in intermediate-to-surface heat transfer, recommending implementation of shear turbulence closure schemes or dynamic mixed-layer penetration mechanisms; (3) Residual overestimation of AW core temperature (0–1°C) and errors in seasonal Atlantification phase (Figs. 8–10, 13), reflecting constraints of mesoscale parameterization on water mass transformation, necessitating development of depth-dependent eddy energy dissipation parameterizations; (4) Asymmetries in regional decadal thermohaline evolution (e.g., underestimated upper-layer warming and overestimated deep warming in the Eurasian Basin, unresolved mid-layer warming and upper-layer freshening trends in the Amerasian Basin; Fig. 13), potentially arising from inadequate resolution of key gateways (e.g., Fram Strait) and oversimplified parameterizations of shelf-basin interactions, demanding optimization through nested grids or regional mesh refinement.

This study confirms that E3SMv2-MPAS significantly enhances simulation capabilities for Arctic oceanic thermal structures and cross-layer coupling processes through integration of high-resolution unstructured meshes with optimized physical parameterization schemes, establishing crucial technical references for polar climate model development in the CMIP7 era.

https://doi.org/10.5194/egusphere-2025-2665
Preprint. Discussion started: 10 July 2025

However, persistent biases highlight remaining challenges in mesoscale process representation and boundary flux constraints. Future priorities include: (1) Development of process-oriented parameterizations enabling eddy-mixing-stratification feedback coupling; (2) Implementation of Arctic-focused data assimilation systems to reduce boundary forcing uncertainties; (3) Execution of perturbed-parameter ensemble experiments to quantify sensitivity thresholds. Such improvements will enhance predictive capabilities for Arctic amplification and tipping point dynamics, ultimately supporting evidence-based climate governance.

Code and data availability. The E3SM model code is publicly available via the https://github.com/E3SM-Project/E3SM/releases. Instructions on how to configure and execute E3SM are available at https://e3sm.org/model/running-e3sm/e3sm-quick-start/. All simulations detailed in Section 2.1 can be regenerated by executing the code hosted in this repository: https://doi.org/10.5281/zenodo.15493256 (Lv, 2025). Preprocessing of E3SMv2-MPAS outputs utilized nco-5.1.1, accessible through the https://nco.sourceforge.net/. The JRA55-v1.5 atmospheric forcing data driving the simulations were obtained from the https://aims2.llnl.gov/search/input4mips/. ETOPO 2022 bathymetry was derived from the https://www.ncei.noaa.gov/products/etopo-global-relief-model. Model evaluations employed the following observational and reanalysis products: Sea ice concentration: NSIDC (https://noaadata.apps.nsidc.org/NOAA/G02202_V4/north/aggregate/), Met Office Hadley Centre observational datasets (https://www.metoffice.gov.uk/hadobs/), and ERA5 monthly single-level data (https://cds.climate.copernicus.eu/datasets/reanalysis-era5-single-levels-monthly-means?tab=overview); Sea ice thickness: PIOMAS (http://psc.apl.uw.edu/research/projects/arctic-sea-ice-volume-anomaly/data/model_grid), PIOMAS-20C reconstruction (https://psc.apl.uw.edu/research/projects/piomas-20c/) and ICESat/ICESat-2 L4 gridded products (https://nsidc.org/data/issitgr4/versions/1 and https://nsidc.org/data/is2sitmogr4/versions/3); Sea surface properties: OISST (https://www.ncei.noaa.gov/products/optimum-interpolation-sst) and OISSS (https://www.esr.org/data-products/oisss/overview/); Oceanographic profiles: WOA2023 (https://www.ncei.noaa.gov/products/world-ocean-atlas), EN.4.2.2 objective analyzes (https://www.metoffice.gov.uk/hadobs/en4/). In situ observational profiles from four key Arctic regions (the western/eastern Eurasian Basin, the Chukchi Sea, and the Beaufort Sea), vertical profiles from 13 CMIP6 models, thermohaline profiles and Atlantic Water core temperature outputs from five OMIP2 ensemble groups, along with E3SM-Arctic-OSI simulations and Atlantic Water core temperature and depth observational benchmarks, are described in the main text. Detailed metadata specifications and data access instructions for these datasets are provided in the corresponding references cited therein.

https://doi.org/10.5194/egusphere-2025-2665
Preprint. Discussion started: 10 July 2025

Author contributions. XL led the manuscript writing and paper analysis. XL, YC, and HD performed the installation, configuration, and execution of the E3SMv2-MPAS model. HW, KR, and YW were primarily responsible for the conceptualization of the study and manuscript revisions. All co-authors reviewed and commented on the final version of the manuscript.

Competing interests. No competing interests are present.

Acknowledgments. The public availability of different observational data sets and reanalysis data used in this work is a great help for model development, so the efforts of respective working groups are appreciated. This work was supported by the National Key R&D Program of China (Grant No. 2021YFC3101503), the Science and Technology Innovation Program of Hunan Province (Grant No.2022RC3070), the National Natural Science Foundation of China (Grant No. 42305176), the Hunan Provincial Natural Science Foundation of China (Grant No. 2023JJ10053), the National Natural Science Foundation of China (Grant No. 42276205) and the Hunan Provincial Science and Technology Innovation Leading Talent Fund.

https://doi.org/10.5194/egusphere-2025-2665
Preprint. Discussion started: 10 July 2025

References

Aagaard, K., Coachman, L. K., and Carmack, E.: On the halocline of the Arctic Ocean, Deep-Sea Res. Pt. A, 28, 529–545, https://doi.org/10.1016/0198-0149(81)90115-1, 1981.

Aksenov, Y., Karcher, M., Proshutinsky, A., Gerdes, R., De Cuevas, B., Golubeva, E., Kauker, F., Nguyen, A. T., Platov, G. A., Wadley, M., Watanabe, E., Coward, A. C., and Nurser, A. J. G.: Arctic pathways of P acific W ater: Arctic O cean M odel I ntercomparison experiments, J. Geophys. Res.-Oceans, 121, 27–59, https://doi.org/10.1002/2015JC011299, 2016.

Calvin, K., Dasgupta, D., Krinner, G., Mukherji, A., Thorne, P. W., Trisos, C., Romero, J., Aldunce, P., Barrett, K., Blanco, G., Cheung, W. W. L., Connors, S., Denton, F., Diongue-Niang, A., Dodman, D., Garschagen, M., Geden, O., Hayward, B., Jones, C., Jotzo, F., Krug, T., Lasco, R., Lee, Y.-Y., Masson-Delmotte, V., Meinshausen, M., Mintenbeck, K., Mokssit, A., Otto, F. E. L., Pathak, M., Pirani, A., Poloczanska, E., Pörtner, H.-O., Revi, A., Roberts, D. C., Roy, J., Ruane, A. C., Skea, J., Shukla, P. R., Slade, R., Slangen, A., Sokona, Y., Sörensson, A. A., Tignor, M., Van Vuuren, D., Wei, Y.-M., Winkler, H., Zhai, P., Zommers, Z., Hourcade, J.-C., Johnson, F. X., Pachauri, S., Simpson, N. P., Singh, C., Thomas, A., Totin, E., Arias, P., Bustamante, M., Elgizouli, I., Flato, G., Howden, M., Méndez-Vallejo, C., Pereira, J. J., Pichs-Madruga, R., Rose, S. K., Saheb, Y., Sánchez Rodríguez, R., Ürge-Vorsatz, D., Xiao, C., Yassaa, N., Alegría, A., Armour, K., Bednar-Friedl, B., Blok, K., Cissé, G., Dentener, F., Eriksen, S., Fischer, E., Garner, G., Guivarch, C., Haasnoot, M., Hansen, G., Hauser, M., Hawkins, E., Hermans, T., Kopp, R., Leprince-Ringuet, N., Lewis, J., Ley, D., Ludden, C., Niamir, L., Nicholls, Z., Some, S., Szopa, S., Trewin, B., Van Der Wijst, K.-I., Winter, G., Witting, M., Birt, A., Ha, M., et al.: IPCC, 2023: Climate Change 2023: Synthesis Report. Contribution of Working Groups I, II and III to the Sixth Assessment Report of the Intergovernmental Panel on Climate Change [Core Writing Team, H. Lee and J. Romero (eds.)]. IPCC, Geneva, Switzerland., Intergovernmental Panel on Climate Change (IPCC), https://doi.org/10.59327/IPCC/AR6-9789291691647, 2023.

Canuto, V. M., Howard, A., Cheng, Y., and Dubovikov, M. S.: Ocean Turbulence. Part I: One-Point Closure Model—Momentum and Heat Vertical Diffusivities, J. Phys. Oceanogr., 31, 1413–1426, https://doi.org/10.1175/1520-0485(2001)031<1413:OTPIOP>2.0.CO;2, 2001.

Carmack, E., Winsor, P., and Williams, W.: The contiguous panarctic Riverine Coastal Domain: A unifying concept, Prog. Oceanogr., 139, 13–23, https://doi.org/10.1016/j.pocean.2015.07.014, 2015a.

Carmack, E., Polyakov, I., Padman, L., Fer, I., Hunke, E., Hutchings, J., Jackson, J., Kelley, D., Kwok, R., Layton, C., Melling, H., Perovich, D., Persson, O., Ruddick, B., Timmermans, M.-L., Toole, J., Ross, T., Vavrus, S., and Winsor, P.: Toward Quantifying the Increasing Role of Oceanic Heat in Sea Ice Loss in the New Arctic, Bull. Am. Meteorol. Soc., 96, 2079–2105, https://doi.org/10.1175/BAMS-D-13-00177.1, 2015b.

Chen, C., Gao, G., Zhang, Y., Beardsley, R. C., Lai, Z., Qi, J., and Lin, H.: Circulation in the Arctic Ocean: Results from a high-resolution coupled ice-sea nested Global-FVCOM and Arctic-FVCOM system, Prog. Oceanogr., 141, 60–80, https://doi.org/10.1016/j.pocean.2015.12.002, 2016.

Danilov, S., Sidorenko, D., Wang, Q., and Jung, T.: The Finite-volumE Sea ice–Ocean Model (FESOM2), Geosci. Model Dev., 10, 765–789, https://doi.org/10.5194/gmd-10-765-2017, 2017.

Davis, P. E. D., Lique, C., Johnson, H. L., and Guthrie, J. D.: Competing Effects of Elevated Vertical Mixing and Increased Freshwater Input on the Stratification and Sea Ice Cover in a Changing Arctic Ocean, J. Phys. Oceanogr., 46, 1531–1553, https://doi.org/10.1175/JPO-D-15-0174.1, 2016.

Duarte, P., Sundfjord, A., Meyer, A., Hudson, S. R., Spreen, G., and Smedsrud, L. H.: Warm Atlantic Water Explains Observed Sea Ice Melt Rates North of Svalbard, J. Geophys. Res.-Oceans, 125, e2019JC015662, https://doi.org/10.1029/2019JC015662, 2020.

https://doi.org/10.5194/egusphere-2025-2665
Preprint. Discussion started: 10 July 2025

Fu, C., Pennelly, C., Garcia-Quintana, Y., and Myers, P. G.: Pulses of Cold Atlantic Water in the Arctic Ocean From an Ocean Model Simulation, J. Geophys. Res.-Oceans, 128, e2023JC019663, https://doi.org/10.1029/2023JC019663, 2023.

Gent, P. R. and Mcwilliams, J. C.: Isopycnal Mixing in Ocean Circulation Models, J. Phys. Oceanogr., 20, 150–155, https://doi.org/10.1175/1520-0485(1990)020%3C0150:IMIOCM%3E2.0.CO;2, 1990.

Golaz, J., Caldwell, P. M., Van Roekel, L. P., Petersen, M. R., Tang, Q., Wolfe, J. D., Abeshu, G., Anantharaj, V., Asay-Davis, X. S., Bader, D. C., Baldwin, S. A., Bisht, G., Bogenschutz, P. A., Branstetter, M., Brunke, M. A., Brus, S. R., Burrows, S. M., Cameron-Smith, P. J., Donahue, A. S., Deakin, M., Easter, R. C., Evans, K. J., Feng, Y., Flanner, M., Foucar, J. G., Fyke, J. G., Griffin, B. M., Hannay, C., Harrop, B. E., Hoffman, M. J., Hunke, E. C., Jacob, R. L., Jacobsen, D. W., Jeffery, N., Jones, P. W., Keen, N. D., Klein, S. A., Larson, V. E., Leung, L. R., Li, H., Lin, W., Lipscomb, W. H., Ma, P., Mahajan, S., Maltrud, M. E., Mametjanov, A., McClean, J. L., McCoy, R. B., Neale, R. B., Price, S. F., Qian, Y., Rasch, P. J., Reeves Eyre, J. E. J., Riley, W. J., Ringler, T. D., Roberts, A. F., Roesler, E. L., Salinger, A. G., Shaheen, Z., Shi, X., Singh, B., Tang, J., Taylor, M. A., Thornton, P. E., Turner, A. K., Veneziani, M., Wan, H., Wang, H., Wang, S., Williams, D. N., Wolfram, P. J., Worley, P. H., Xie, S., Yang, Y., Yoon, J., Zelinka, M. D., Zender, C. S., Zeng, X., Zhang, C., Zhang, K., Zhang, Y., Zheng, X., Zhou, T., and Zhu, Q.: The DOE E3SM Coupled Model Version 1: Overview and Evaluation at Standard Resolution, J. Adv. Model. Earth Sy., 11, 2089–2129, https://doi.org/10.1029/2018MS001603, 2019.

Golaz, J., Van Roekel, L. P., Zheng, X., Roberts, A. F., Wolfe, J. D., Lin, W., Bradley, A. M., Tang, Q., Maltrud, M. E., Forsyth, R. M., Zhang, C., Zhou, T., Zhang, K., Zender, C. S., Wu, M., Wang, H., Turner, A. K., Singh, B., Richter, J. H., Qin, Y., Petersen, M. R., Mametjanov, A., Ma, P., Larson, V. E., Krishna, J., Keen, N. D., Jeffery, N., Hunke, E. C., Hannah, W. M., Guba, O., Griffin, B. M., Feng, Y., Engwirda, D., Di Vittorio, A. V., Dang, C., Conlon, L. M., Chen, C., Brunke, M. A., Bisht, G., Benedict, J. J., Asay-Davis, X. S., Zhang, Y., Zhang, M., Zeng, X., Xie, S., Wolfram, P. J., Vo, T., Veneziani, M., Tesfa, T. K., Sreepathi, S., Salinger, A. G., Reeves Eyre, J. E. J., Prather, M. J., Mahajan, S., Li, Q., Jones, P. W., Jacob, R. L., Huebler, G. W., Huang, X., Hillman, B. R., Harrop, B. E., Foucar, J. G., Fang, Y., Comeau, D. S., Caldwell, P. M., Bartoletti, T., Balaguru, K., Taylor, M. A., McCoy, R. B., Leung, L. R., and Bader, D. C.: The DOE E3SM Model Version 2: Overview of the Physical Model and Initial Model Evaluation, J. Adv. Model. Earth Sy., 14, e2022MS003156, https://doi.org/10.1029/2022MS003156, 2022.

Good, S. A., Martin, M. J., and Rayner, N. A.: EN4: Quality controlled ocean temperature and salinity profiles and monthly objective analyses with uncertainty estimates, J. Geophys. Res.-Oceans, 118, 6704–6716, https://doi.org/10.1002/2013JC009067, 2013.

Hall, S. B., Subrahmanyam, B., and Morison, J. H.: Intercomparison of Salinity Products in the Beaufort Gyre and Arctic Ocean, Remote Sens., 14, 71, https://doi.org/10.3390/rs14010071, 2021.

Hersbach, H., Bell, B., Berrisford, P., Hirahara, S., Horányi, A., Muñoz-Sabater, J., Nicolas, J., Peubey, C., Radu, R., Schepers, D., Simmons, A., Soci, C., Abdalla, S., Abellan, X., Balsamo, G., Bechtold, P., Biavati, G., Bidlot, J., Bonavita, M., Chiara, G., Dahlgren, P., Dee, D., Diamantakis, M., Dragani, R., Flemming, J., Forbes, R., Fuentes, M., Geer, A., Haimberger, L., Healy, S., Hogan, R. J., Hólm, E., Janisková, M., Keeley, S., Laloyaux, P., Lopez, P., Lupu, C., Radnoti, G., Rosnay, P., Rozum, I., Vamborg, F., Villaume, S., and Thépaut, J.: The ERA5 global reanalysis, Q. J. R. Meteorol. Soc., 146, 1999–2049, https://doi.org/10.1002/qj.3803, 2020.

Heuzé, C., Zanowski, H., Karam, S., and Muilwijk, M.: The Deep Arctic Ocean and Fram Strait in CMIP6 Models, J. Clim., 36, 2551–2584, https://doi.org/10.1175/JCLI-D-22-0194.1, 2023.

Hinrichs, C., Wang, Q., Koldunov, N., Mu, L., Semmler, T., Sidorenko, D., and Jung, T.: Atmospheric Wind Biases: A Challenge for Simulating the Arctic Ocean in Coupled Models?, J. Geophys. Res.-Oceans, 126, e2021JC017565, https://doi.org/10.1029/2021JC017565, 2021.

https://doi.org/10.5194/egusphere-2025-2665
Preprint. Discussion started: 10 July 2025

Hoch, K. E., Petersen, M. R., Brus, S. R., Engwirda, D., Roberts, A. F., Rosa, K. L., and Wolfram, P. J.: MPAS-Ocean Simulation Quality for Variable-Resolution North American Coastal Meshes, J. Adv. Model. Earth Sy., 12, e2019MS001848, https://doi.org/10.1029/2019MS001848, 2020.

Holloway, G., Dupont, F., Golubeva, E., Häkkinen, S., Hunke, E., Jin, M., Karcher, M., Kauker, F., Maltrud, M., Morales Maqueda, M. A., Maslowski, W., Platov, G., Stark, D., Steele, M., Suzuki, T., Wang, J., and Zhang, J.: Water properties and circulation in Arctic Ocean models, J. Geophys. Res., 112, 2006JC003642, https://doi.org/10.1029/2006JC003642, 2007.

Huang, B., Liu, C., Banzon, V., Freeman, E., Graham, G., Hankins, B., Smith, T., and Zhang, H.-M.: Improvements of the Daily Optimum Interpolation Sea Surface Temperature (DOISST) Version 2.1, J. Clim., 34, 2923–2939, https://doi.org/10.1175/JCLI-D-20-0166.1, 2021.

Ilıcak, M., Drange, H., Wang, Q., Gerdes, R., Aksenov, Y., Bailey, D., Bentsen, M., Biastoch, A., Bozec, A., Böning, C., Cassou, C., Chassignet, E., Coward, A. C., Curry, B., Danabasoglu, G., Danilov, S., Fernandez, E., Fogli, P. G., Fujii, Y., Griffies, S. M., Iovino, D., Jahn, A., Jung, T., Large, W. G., Lee, C., Lique, C., Lu, J., Masina, S., George Nurser, A. J., Roth, C., Salas Y Mélia, D., Samuels, B. L., Spence, P., Tsujino, H., Valcke, S., Voldoire, A., Wang, X., and Yeager, S. G.: An assessment of the Arctic Ocean in a suite of interannual CORE-II simulations. Part III: Hydrography and fluxes, Ocean Model., 100, 141–161, https://doi.org/10.1016/j.ocemod.2016.02.004, 2016.

Karami, M. P., Myers, P. G., De Vernal, A., Tremblay, L. B., and Hu, X.: The role of Arctic gateways on sea ice and circulation in the Arctic and North Atlantic Oceans: a sensitivity study with an ocean-sea-ice model, Clim. Dyn., 57, 2129–2151, https://doi.org/10.1007/s00382-021-05798-6, 2021.

Kelly, S. J., Proshutinsky, A., Popova, E. K., Aksenov, Y. K., and Yool, A.: On the Origin of Water Masses in the Beaufort Gyre, J. Geophys. Res.-Oceans, 124, 4696–4709, https://doi.org/10.1029/2019JC015022, 2019.

Khosravi, N., Wang, Q., Koldunov, N., Hinrichs, C., Semmler, T., Danilov, S., and Jung, T.: The Arctic Ocean in CMIP6 Models: Biases and Projected Changes in Temperature and Salinity, Earths Future, 10, e2021EF002282, https://doi.org/10.1029/2021EF002282, 2022.

Kwok, R.: Arctic sea ice thickness, volume, and multiyear ice coverage: losses and coupled variability (1958–2018), Environ. Res. Lett., 13, 105005, https://doi.org/10.1088/1748-9326/aae3ec, 2018.

Landrum, L. and Holland, M. M.: Extremes become routine in an emerging new Arctic, Nat. Clim. Chang., 10, 1108–1115, https://doi.org/10.1038/s41558-020-0892-z, 2020.

Large, W. G., McWilliams, J. C., and Doney, S. C.: Oceanic vertical mixing: A review and a model with a nonlocal boundary layer parameterization, Rev. Geophys., 32, 363–403, https://doi.org/10.1029/94RG01872, 1994.

Laxon, S. W., Giles, K. A., Ridout, A. L., Wingham, D. J., Willatt, R., Cullen, R., Kwok, R., Schweiger, A., Zhang, J., Haas, C., Hendricks, S., Krishfield, R., Kurtz, N., Farrell, S., and Davidson, M.: CryoSat-2 estimates of Arctic sea ice thickness and volume, Geophys. Res. Lett., 40, 732–737, https://doi.org/10.1002/grl.50193, 2013.

Liang, X. and Losch, M.: On the Effects of Increased Vertical Mixing on the Arctic Ocean and Sea Ice, J. Geophys. Res.-Oceans, 123, 9266–9282, https://doi.org/10.1029/2018JC014303, 2018.

Lind, S., Ingvaldsen, R. B., and Furevik, T.: Arctic warming hotspot in the northern Barents Sea linked to declining sea-ice import, Nat. Clim. Chang., 8, 634–639, https://doi.org/10.1038/s41558-018-0205-y, 2018.

Liu, W., Liu, Y., and Zhao, S.: Global mode simulation results comparison between icosahedron spherical mesh and latitude-longitude mesh in China, J. Nanjing Univ. Inf. Sci. Technol. Nat. Sci. Ed., 8, 146–151, https://doi.org/10.13878/j.cnki.jnuist.2016.02.006, 2016.

Locarnini, R. A., Mishonov, A. V., Baranova, O. K., Reagan, J. R., Boyer, T. P., Seidov, D., Wang, Z., Garcia, H. E., Bouchard, C., Cross, S. L., Paver, C. R., and Dukhovskoy, D.: World Ocean Atlas 2023, Volume 1: Temperature, https://doi.org/10.25923/54BH-1613, 2024.

Long, M., Zhang, L., Hu, S., and Qian, S.: Multi-Aspect Assessment of CMIP6 Models for Arctic Sea Ice Simulation, J. Clim., 34, 1515–1529, https://doi.org/10.1175/JCLI-D-20-0522.1, 2021.

Long, Z., Perrie, W., Zhang, M., and Liu, Y.: Responses of Atlantic Water Inflow Through Fram Strait to Arctic Storms, Geophys. Res. Lett., 51, e2023GL107777, https://doi.org/10.1029/2023GL107777, 2024.

Lv, X. (2025). E3SMv2-MPAS. Zenodo. https://doi.org/10.5281/zenodo.15493256

Meier, W., Fetterer, F., Windnagel, A., and Stewart, S.: NOAA/NSIDC Climate Data Record of Passive Microwave Sea Ice Concentration, Version 4, https://doi.org/10.7265/EFMZ-2T65, 2021.

Melnichenko, O., Hacker, P., Maximenko, N., Lagerloef, G., and Potemra, J.: Optimum interpolation analysis of A quarius sea surface salinity, J. Geophys. Res.-Oceans, 121, 602–616, https://doi.org/10.1002/2015JC011343, 2016.

Meyer, A., Fer, I., Sundfjord, A., and Peterson, A. K.: Mixing rates and vertical heat fluxes north of Svalbard from Arctic winter to spring, J. Geophys. Res.-Oceans, 122, 4569–4586, https://doi.org/10.1002/2016JC012441, 2017.

Muilwijk, M., Nummelin, A., Heuzé, C., Polyakov, I. V., Zanowski, H., and Smedsrud, L. H.: Divergence in Climate Model Projections of Future Arctic Atlantification, J. Clim., 36, 1727–1748, https://doi.org/10.1175/JCLI-D-22-0349.1, 2023.

Nurser, A. J. G. and Bacon, S.: The Rossby radius in the Arctic Ocean, Ocean Sci., 10, 967–975, https://doi.org/10.5194/os-10-967-2014, 2014.

Onarheim, I. H., Eldevik, T., Smedsrud, L. H., and Stroeve, J. C.: Seasonal and Regional Manifestation of Arctic Sea Ice Loss, J. Clim., 31, 4917–4932, https://doi.org/10.1175/JCLI-D-17-0427.1, 2018.

Pan, R., Shu, Q., Wang, Q., Wang, S., Song, Z., He, Y., and Qiao, F.: Future Arctic Climate Change in CMIP6 Strikingly Intensified by NEMO-Family Climate Models, Geophys. Res. Lett., 50, e2022GL102077, https://doi.org/10.1029/2022GL102077, 2023.

Peralta-Ferriz, C. and Woodgate, R. A.: Seasonal and interannual variability of pan-Arctic surface mixed layer properties from 1979 to 2012 from hydrographic data, and the dominance of stratification for multiyear mixed layer depth shoaling, Prog. Oceanogr., 134, 19–53, https://doi.org/10.1016/j.pocean.2014.12.005, 2015.

Petty, A. A., Kurtz, N. T., Kwok, R., Markus, T., and Neumann, T. A.: Winter Arctic Sea Ice Thickness From ICESat-2 Freeboards, J. Geophys. Res.-Oceans, 125, e2019JC015764, https://doi.org/10.1029/2019JC015764, 2020.

Petty, A. A., Kurtz, N., Kwok, R., Markus, T., Neumann, T. A., and Keeney, N.: ICESat-2 L4 Monthly Gridded Sea Ice Thickness. (IS2SITMOGR4, Version 3). [Data Set]., https://doi.org/10.5067/ZCSU8Y5U1BQW, 2023.

Polyakov, I. V., Timokhov, L. A., Alexeev, V. A., Bacon, S., Dmitrenko, I. A., Fortier, L., Frolov, I. E., Gascard, J.-C., Hansen, E., Ivanov, V. V., Laxon, S., Mauritzen, C., Perovich, D., Shimada, K., Simmons, H. L., Sokolov, V. T., Steele, M.,

https://doi.org/10.5194/egusphere-2025-2665
Preprint. Discussion started: 10 July 2025

and Toole, J.: Arctic Ocean Warming Contributes to Reduced Polar Ice Cap, J. Phys. Oceanogr., 40, 2743–2756, https://doi.org/10.1175/2010JPO4339.1, 2010.

Polyakov, I. V., Pnyushkov, A. V., Alkire, M. B., Ashik, I. M., Baumann, T. M., Carmack, E. C., Goszczko, I., Guthrie, J., Ivanov, V. V., Kanzow, T., Krishfield, R., Kwok, R., Sundfjord, A., Morison, J., Rember, R., and Yulin, A.: Greater role for Atlantic inflows on sea-ice loss in the Eurasian Basin of the Arctic Ocean, Science, 356, 285–291, https://doi.org/10.1126/science.aai8204, 2017.

Polyakov, I. V., Alkire, M. B., Bluhm, B. A., Brown, K. A., Carmack, E. C., Chierici, M., Danielson, S. L., Ellingsen, I., Ershova, E. A., Gårdfeldt, K., Ingvaldsen, R. B., Pnyushkov, A. V., Slagstad, D., and Wassmann, P.: Borealization of the Arctic Ocean in Response to Anomalous Advection From Sub-Arctic Seas, Front. Mar. Sci., 7, 491, https://doi.org/10.3389/fmars.2020.00491, 2020a.

Polyakov, I. V., Rippeth, T. P., Fer, I., Alkire, M. B., Baumann, T. M., Carmack, E. C., Ingvaldsen, R., Ivanov, V. V., Janout, M., Lind, S., Padman, L., Pnyushkov, A. V., and Rember, R.: Weakening of Cold Halocline Layer Exposes Sea Ice to Oceanic Heat in the Eastern Arctic Ocean, J. Clim., 33, 8107–8123, https://doi.org/10.1175/JCLI-D-19-0976.1, 2020b.

Polyakov, I. V., Mayer, M., Tietsche, S., and Karpechko, A. Yu.: Climate Change Fosters Competing Effects of Dynamics and Thermodynamics in Seasonal Predictability of Arctic Sea Ice, J. Clim., 35, 2849–2865, https://doi.org/10.1175/JCLI-D-21-0463.1, 2022.

Rayner, N. A., Parker, D. E., Horton, E. B., Folland, C. K., Alexander, L. V., Rowell, D. P., Kent, E. C., and Kaplan, A.: Global analyses of sea surface temperature, sea ice, and night marine air temperature since the late nineteenth century, J. Geophys. Res., 108, 2002JD002670, https://doi.org/10.1029/2002JD002670, 2003.

Reagan, J. R., Seidov, D., Wang, Z., Dukhovskoy, D., Boyer, T. P., Locarnini, R. A., Baranova, O. K., Mishonov, A. V., Garcia, H. E., Bouchard, C., Cross, S. L., and Paver, C. R.: World Ocean Atlas 2023, Volume 2: Salinity, https://doi.org/10.25923/70QT-9574, 2024.

Richards, A. E., Johnson, H. L., and Lique, C.: Spatial and Temporal Variability of Atlantic Water in the Arctic From 40 Years of Observations, J. Geophys. Res.-Oceans, 127, e2021JC018358, https://doi.org/10.1029/2021JC018358, 2022.

Ringler, T., Petersen, M., Higdon, R. L., Jacobsen, D., Jones, P. W., and Maltrud, M.: A multi-resolution approach to global ocean modeling, Ocean Model., 69, 211–232, https://doi.org/10.1016/j.ocemod.2013.04.010, 2013.

Scholz, P., Sidorenko, D., Gurses, O., Danilov, S., Koldunov, N., Wang, Q., Sein, D., Smolentseva, M., Rakowsky, N., and Jung, T.: Assessment of the Finite-volumE Sea ice-Ocean Model (FESOM2.0) – Part 1: Description of selected key model elements and comparison to its predecessor version, Geosci. Model Dev., 12, 4875–4899, https://doi.org/10.5194/gmd-12-4875-2019, 2019.

Schweiger, A., Lindsay, R., Zhang, J., Steele, M., Stern, H., and Kwok, R.: Uncertainty in modeled Arctic sea ice volume, J. Geophys. Res., 116, C00D06, https://doi.org/10.1029/2011JC007084, 2011.

Schweiger, A. J., Wood, K. R., and Zhang, J.: Arctic Sea Ice Volume Variability over 1901–2010: A Model-Based Reconstruction, J. Clim., 32, 4731–4752, https://doi.org/10.1175/JCLI-D-19-0008.1, 2019.

Shu, Q., Wang, Q., Su, J., Li, X., and Qiao, F.: Assessment of the Atlantic water layer in the Arctic Ocean in CMIP5 climate models, Clim. Dyn., 53, 5279–5291, https://doi.org/10.1007/s00382-019-04870-6, 2019.

https://doi.org/10.5194/egusphere-2025-2665
Preprint. Discussion started: 10 July 2025

Shu, Q., Wang, Q., Årthun, M., Wang, S., Song, Z., Zhang, M., and Qiao, F.: Arctic Ocean Amplification in a warming climate in CMIP6 models, Sci. Adv., 8, eabn9755, https://doi.org/10.1126/sciadv.abn9755, 2022.

Smagorinsky, J.: GENERAL CIRCULATION EXPERIMENTS WITH THE PRIMITIVE EQUATIONS: I. THE BASIC EXPERIMENT*, Mon. Wea. Rev., 91, 99–164, https://doi.org/10.1175/1520-0493(1963)091<0099:GCEWTP>2.3.CO;2, 1963.

Steele, M. and Boyd, T.: Retreat of the cold halocline layer in the Arctic Ocean, J. Geophys. Res., 103, 10419–10435, https://doi.org/10.1029/98JC00580, 1998.

Steele, M., Morley, R., and Ermold, W.: PHC: A Global Ocean Hydrography with a High-Quality Arctic Ocean, J. Clim., 14, 2079–2087, https://doi.org/10.1175/1520-0442(2001)014<2079:PAGOHW>2.0.CO;2, 2001.

Stroeve, J., Barrett, A., Serreze, M., and Schweiger, A.: Using records from submarine, aircraft and satellites to evaluate climate model simulations of Arctic sea ice thickness, Cryosphere, 8, 1839–1854, https://doi.org/10.5194/tc-8-1839-2014, 2014.

Tian, Z., Liang, X., Zhang, J., Bi, H., Zhao, F., and Li, C.: Thermodynamical and Dynamical Impacts of an Intense Cyclone on Arctic Sea Ice, J. Geophys. Res.-Oceans, 127, e2022JC018436, https://doi.org/10.1029/2022JC018436, 2022.

Tsujino, H., Urakawa, S., Nakano, H., Small, R. J., Kim, W. M., Yeager, S. G., Danabasoglu, G., Suzuki, T., Bamber, J. L., Bentsen, M., Böning, C. W., Bozec, A., Chassignet, E. P., Curchitser, E., Boeira Dias, F., Durack, P. J., Griffies, S. M., Harada, Y., Ilicak, M., Josey, S. A., Kobayashi, C., Kobayashi, S., Komuro, Y., Large, W. G., Le Sommer, J., Marsland, S. J., Masina, S., Scheinert, M., Tomita, H., Valdivieso, M., and Yamazaki, D.: JRA-55 based surface dataset for driving ocean–sea-ice models (JRA55-do), Ocean Model., 130, 79–139, https://doi.org/10.1016/j.ocemod.2018.07.002, 2018.

Turner, A. K., Lipscomb, W. H., Hunke, E. C., Jacobsen, D. W., Jeffery, N., Engwirda, D., Ringler, T. D., and Wolfe, J. D.: MPAS-Seaice (v1.0.0): sea-ice dynamics on unstructured Voronoi meshes, Geosci. Model Dev., 15, 3721–3751, https://doi.org/10.5194/gmd-15-3721-2022, 2022.

Turner, J. S.: The Melting of Ice in the Arctic Ocean: The Influence of Double-Diffusive Transport of Heat from Below, J. Phys. Oceanogr., 40, 249–256, https://doi.org/10.1175/2009JPO4279.1, 2010.

Veneziani, M., Maslowski, W., Lee, Y. J., D'Angelo, G., Osinski, R., Petersen, M. R., Weijer, W., Craig, A. P., Wolfe, J. D., Comeau, D., and Turner, A. K.: An evaluation of the E3SMv1 Arctic ocean and sea-ice regionally refined model, Geosci. Model Dev., 15, 3133–3160, https://doi.org/10.5194/gmd-15-3133-2022, 2022.

Wang, Q., Wekerle, C., Danilov, S., Wang, X., and Jung, T.: A 4.5 km resolution Arctic Ocean simulation with the global multi-resolution model FESOM 1.4, Geosci. Model Dev., 11, 1229–1255, https://doi.org/10.5194/gmd-11-1229-2018, 2018.

Wang, Q., Shu, Q., Wang, S., Beszczynska-Moeller, A., Danilov, S., Steur, L., Haine, T. W. N., Karcher, M., Lee, C. M., Myers, P. G., Polyakov, I. V., Provost, C., Skagseth, Ø., Spreen, G., and Woodgate, R.: A Review of Arctic–Subarctic Ocean Linkages: Past Changes, Mechanisms, and Future Projections, Ocean-Land-Atmos. Res., 2, 0013, https://doi.org/10.34133/olar.0013, 2023.

Wang, Q., Shu, Q., Bozec, A., Chassignet, E. P., Fogli, P. G., Fox-Kemper, B., Hogg, A. McC., Iovino, D., Kiss, A. E., Koldunov, N., Le Sommer, J., Li, Y., Lin, P., Liu, H., Polyakov, I., Scholz, P., Sidorenko, D., Wang, S., and Xu, X.: Impact of increased resolution on Arctic Ocean simulations in Ocean Model Intercomparison Project phase 2 (OMIP-2), Geosci. Model Dev., 17, 347–379, https://doi.org/10.5194/gmd-17-347-2024, 2024.

https://doi.org/10.5194/egusphere-2025-2665
Preprint. Discussion started: 10 July 2025

Wassmann, P., Kosobokova, K. N., Slagstad, D., Drinkwater, K. F., Hopcroft, R. R., Moore, S. E., Ellingsen, I., Nelson, R. J., Carmack, E., Popova, E., and Berge, J.: The contiguous domains of Arctic Ocean advection: Trails of life and death, Prog. Oceanogr., 139, 42–65, https://doi.org/10.1016/j.pocean.2015.06.011, 2015.

Wekerle, C., Wang, Q., Danilov, S., Jung, T., and Schröter, J.: The Canadian Arctic Archipelago throughflow in a multiresolution global model: Model assessment and the driving mechanism of interannual variability, J. Geophys. Res.-Oceans, 118, 4525–4541, https://doi.org/10.1002/jgrc.20330, 2013.

Zhang, J. and Rothrock, D. A.: Modeling Global Sea Ice with a Thickness and Enthalpy Distribution Model in Generalized Curvilinear Coordinates, Mon. Wea. Rev., 131, 845–861, https://doi.org/10.1175/1520-0493(2003)131<0845:MGSIWA>2.0.CO;2, 2003.

Zhang, Y., Chen, C., Beardsley, R. C., Gao, G., Qi, J., and Lin, H.: Seasonal and interannual variability of the Arctic sea ice: A comparison between AO-FVCOM and observations, J. Geophys. Res.-Oceans, 121, 8320–8350, https://doi.org/10.1002/2016JC011841, 2016.

Zhu, Y., Zhang, R.-H., Moum, J. N., Wang, F., Li, X., and Li, D.: Physics-informed deep-learning parameterization of ocean vertical mixing improves climate simulations, Nat. Sci. Rev., 9, nwac044, https://doi.org/10.1093/nsr/nwac044, 2022.

Zwally, H. J., Schutz, B., Abdalati, W., Abshire, J., Bentley, C., Brenner, A., Bufton, J., Dezio, J., Hancock, D., Harding, D., Herring, T., Minster, B., Quinn, K., Palm, S., Spinhirne, J., and Thomas, R.: ICESat's laser measurements of polar ice, atmosphere, ocean, and land, J. Geodyn., 34, 405–445, https://doi.org/10.1016/s0264-3707(02)00042-x, 2002.